Ambient aerosol properties in the remote atmosphere from global-scale in-situ measurements

Charles A. Brock[1], Karl D. Froyd[1,2], Maximilian Dollner[3], Christina J. Williamson[1,2], Gregory Schill[1,2], Daniel M. Murphy[1], Nicholas J. Wagner[1,2], Agnieszka Kupc[3], Jose L. Jimenez[2,4], Pedro Campuzano-Jost[2,4], Benjamin A. Nault[2,4], Jason C. Schroder[2,4], Douglas A. Day[2,4], Derek J. Price[2,4], Bernadett Weinzierl[3], Joshua P. Schwarz[1], Joseph M. Katich[1,2], Linghan Zeng[5], Rodney Weber[5], Jack Dibb[6], Eric Scheuer[6], Glenn S. Diskin[7], Joshua P. DiGangi[7], ThaoPaul Bui[8], Jonathan M. Dean-Day[9], Chelsea R. Thompson[1,2], Jeff Peischl[1,2], Thomas B. Ryerson[1], Ilann Bourgeois[1,2], Bruce C. Daube[10], Róisín Commane[11,12], Steven C. Wofsy[10]

[1]Chemical Sciences Laboratory, National Oceanic and Atmospheric Administration, Boulder, Colorado 80305, United States
[2]Cooperative Institute for Research in Environmental Sciences, University of Colorado, Boulder, Colorado 80309, United States
[3]Aerosol Physics and Environmental Physics, Faculty of Physics, University of Vienna, 1090 Wien, Austria
[4]Department of Chemistry, University of Colorado, Boulder, Colorado 80309, United States
[5]School of Earth and Atmospheric Sciences, Georgia Institute of Technology, Atlanta, Georgia 30332, United States
[6]Earth Systems Research Center, Institute for the Study of Earth, Oceans, and Space, University of New Hampshire, Durham, New Hampshire 03824, United States
[7]Langley Research Center, National Aeronautics and Space Administration, Hampton, Virginia 23681, United States
[8]Ames Research Center, National Aeronautics and Space Administration, Moffett Field, California 94035, United States
[9]Bay Area Environment Research Institute, Moffett Field, California 94035, United States
[10]Department of Earth and Planetary Sciences, Harvard University, Cambridge, Massachusetts 02138, United States
[11]School of Engineering and Applied Sciences, Harvard University, Cambridge, Massachusetts 02138, United States
[12]Now at: Earth and Environmental Sciences, Lamont-Doherty Earth Observatory, Columbia University, Palisades, New York 10964, United States

Correspondence to: Charles A. Brock (charles.a.brock@noaa.gov)

Abstract. In situ measurements of aerosol microphysical, chemical, and optical properties were made during global-scale flights from 2016-2018 as part of the Atmospheric Tomography Mission (ATom). A NASA DC-8 aircraft flew from ~84 °N to ~86 °S latitude over the Pacific, Atlantic, Arctic, and Southern oceans while profiling nearly continuously between altitudes of ~160 m and ~12 km. These global circuits were made once each season. Particle size distributions measured in the aircraft cabin at dry conditions and with an underwing probe at ambient conditions were combined with bulk and single-particle composition observations and measurements of water vapor, pressure and temperature to estimate aerosol hygroscopicity and hygroscopic growth factors and calculate size distributions at ambient relative humidity. These

reconstructed, composition-resolved ambient size distributions were used to estimate intensive and extensive aerosol

35   properties, including single scatter albedo, asymmetry parameter, extinction, absorption, Ångström exponents, and aerosol

optical depth (AOD) at several wavelengths, as well as CCN concentrations at fixed supersaturations and lognormal fits to

four modes. Dry extinction and absorption were compared with direct, in situ measurements, and AOD derived from the

extinction profiles was compared with remotely sensed AOD measurements from the ground-based Aerosol Robotic

Network (AERONET); these calculated parameters were in agreement with the direct observations within expected

40   uncertainties.

The purpose of this work is to describe the methodology by which ambient aerosol properties are estimated from

the in situ measurements, provide statistical descriptions of the aerosol characteristics of different remote air mass types,

examine the contributions to AOD from different aerosol types in different air masses, and provide an entry point to the

ATom aerosol database. The contributions of different aerosol types (dust, sea salt, biomass burning, etc.) to AOD generally

45   align with expectations based on location of the profiles relative to continental sources of aerosols, with sea salt and aerosol

water dominating the column extinction in most remote environments and dust and biomass burning (BB) particles

contributing substantially to AOD, especially downwind of the African continent. Contributions of dust and BB aerosols to

AOD were also significant in the free troposphere over the North Pacific.

Comparisons of lognormally fitted size distribution parameters to values in a database commonly used in global

50   models show significant differences in the mean diameters and standard deviations for accumulation-mode particles and

coarse-mode dust. In contrast, comparisons of lognormal parameters derived from the ATom data with previously published

ship-borne measurements in the remote marine boundary layer show general agreement.

The dataset resulting from this work can be used to improve global-scale representation of climate-relevant aerosol

properties in remote air masses through comparison with output from global models and with assumptions used in retrievals

55   of aerosol properties from both ground-based and satellite remote sensing.

1 Introduction

Atmospheric aerosols are important components of the atmospheric system, interacting chemically with gas-phase components and affecting climate processes through aerosol-radiation and aerosol-cloud interactions (IPCC, 2013). We use the term "aerosol" to indicate a population of non-cloud (non-activated) particles that are suspended in and interacting with

60 air and its reactive gas-phase constituents. In this terminology, any given air parcel may contain multiple, externally mixed aerosol types (for example a sea-salt aerosol and a dust aerosol may coexist within the same air parcel). Global chemistry-climate models usually represent atmospheric aerosols using bulk, modal, or binned microphysical schemes that apportion various components into size classes. These representations of aerosol properties are often dynamic, allowing for chemical reactions, growth, coagulation, cloud nucleation, in-cloud production, and dry and wet deposition. To effectively simulate

65 the role of atmospheric aerosol in climate processes, models must adequately represent the mass and composition of different aerosol types and their distribution amongst particle sizes, the spatial and temporal distribution of the components, their mixing state (existing as external mixtures with different compositions or internal mixtures with blended compositions), their optical properties (often a function of particle size), and their hygroscopic properties and suitability to serve as cloud condensation nuclei (CCN). Underlying these properties are the physical and chemical processes actually being represented

70 in the simulations, including emissions of particles and gas-phase precursors, atmospheric transport, gas-phase, heterogeneous, and aqueous chemistry, cloud processing, evaporation, wet and dry deposition, and transformations such as condensation and coagulation. Simulating these disparate processes and properties is a challenging task for global-scale models, which must balance detailed, size-dependent representations of these mechanisms against computational efficiency. There is an imperative for improving aerosol representation in global models: the largest source of uncertainty in

75 understanding climate sensitivity remains aerosol-radiation and aerosol-cloud interactions (the direct and indirect effects, respectively).

Global chemistry-climate models often evaluate their performance based on comparison to remote sensing observations from satellites and from ground-based sensors such as the Aerosol Robotic Network (AERONET; Holben et al., 1998). The satellite products most often used are aerosol optical depth (AOD) from sensors such as the Moderate Resolution

80   Imaging Spectroradiometer (MODIS) on NASA's Aqua and Terra satellites, the Multi-angle Imaging Spectroradiometer

(MISR) on Terra, and the Visible Infrared Imaging Radiation Suite (VIIRS) instrument on the Suomi National Polar-orbiting

Partnership satellite. Additional information on aerosol characteristics such as the angular dependence of scattered light (the

phase function) and single scatter albedo ω_0 (the ratio of light scattering to the sum of scattering and absorption) can be

derived from multi-angle techniques such as from AERONET and MISR. In general, algorithms to generate such additional

85   information on aerosol properties from remote sensing measures require *a priori* assumptions about aerosol characteristics

because the retrievals are under-constrained (e.g., Dubovik et al., 2000). In the case of AERONET, aerosol properties such

as column-averaged aerosol phase function and ω_0 can be derived with confidence only in cases where AOD exceeds 0.4

(Dubovik et al., 2000; Holben et al., 2006), much more turbid than is typical of the atmosphere away from large continental

sources of pollution, dust, and biomass burning. Extrapolating intensive aerosol properties such as ω_0 from measurements at

90   high AOD values to cleaner regions may lead to substantial biases (Andrews et al., 2017). In a recent overview paper, Kahn

et al. (2017) stated that "at present, it seems unlikely that particle microphysical and chemical properties can be retrieved

from remote sensing measurements alone at the level of accuracy required to substantially reduce uncertainties in total direct

aerosol radiative forcing (DARF), its anthropogenic component, aerosol–cloud interactions, horizontal material transports,

surface–atmosphere aerosol fluxes, and air quality–related applications."

95   In this work we make use of in situ measurements made on a research aircraft during the ATom project, a series of

global scale, representative (Strode et al., 2018; Katich et al., 2018) tropospheric observations over the remote Pacific and

Atlantic Oceans and portions of the Arctic and Antarctic Oceans, to provide detailed descriptions of the aerosols

encountered. We sampled an airstream through an inlet, dried it, and used in-cabin instruments to determine the

microphysical and chemical characteristics of the dried aerosol. We then calculated the ambient aerosol properties by

100   accounting for hygroscopic growth to ambient humidity, and developed statistics for a number of dry and ambient aerosol

properties for the different air mass types encountered. These data, which cover single transects over the two ocean basins in

each of four seasons, do not represent a climatology of aerosol characteristics, but provide a representatively sampled

"snapshot" of particle properties that can be compared with simulations of these properties to help identify issues in model

output and reveal processes that may be inadequately represented. The overarching goal of this effort is to describe how the

105 in situ measurements are combined into a single, consistent description of the aerosol microphysical, chemical, hygroscopic,

and optical properties listed in Table 1, to present a summary of aerosol properties in different air masses encountered during

ATom, and to provide an entry point to the ATom dataset for use in modeling and remote sensing investigations of

atmospheric composition and climate.

2 Methods

110 ### 2.1 The ATom project

The Atom project was an airborne measurement program that investigated the composition of the remote marine

troposphere over four seasons. Science flights took place from 29 July–23 August 2016, 26 January–21 February 2017, 29

September–27 October 2017, and 24 April–21 May 2018, named ATom-1 through ATom-4, respectively. The NASA DC-8

aircraft, a large, four-engine, intercontinental-range commercial aircraft adapted for scientific measurements (NASA, 2015),

115 flew from southern California southward to near the equator and back, then north to the Arctic Ocean, southward over the

Pacific Ocean to New Zealand, across the Southern Ocean to Chile, northward to the Azores, across the North American

Arctic to Alaska, and back to California (Fig. 1). On ATom-3 and -4, the aircraft flew southward from Chile over the

Antarctic Peninsula and Weddell Sea. On ATom-1, the aircraft flew from Greenland to California without crossing the North

American Arctic to Alaska. The routes northward across the South Atlantic and across eastern Canada and Greenland varied

120 due to airport availability and weather conditions.

During these flights, the DC-8 made repeated en-route ascents and descents from the maximum flight altitude

permitted by aircraft performance and air traffic control (ATC) to within ~160 m of the surface (visibility and ATC

permitting), and back, similar to the HIAPER Pole-to-Pole Observations (HIPPO) study using the smaller National Science

Foundation Gulfstream G-V aircraft (Wofsy, 2011). We consider a total of 639 atmospheric profiles, including both descents

125 and ascents, in this study. The DC-8 maintained level flight for several minutes at the lowest and highest altitudes, and when

required by ATC or to save fuel; at all other times it was constantly ascending or descending at ~450 m min^{-1}. The flight

routes were pre-planned and not adjusted except to avoid hazardous flight conditions such as deep convection. Pre-planned, multi-level flight patterns were made 12 times in the marine boundary layer (MBL) to investigate vertical fluxes over the remote oceans.

2.2 Instruments

The DC-8 aircraft carried a substantial payload of in situ meteorological, gas-phase and aerosol instruments and limited radiation instruments. Measurements included reactive nitrogen compounds, volatile organic compounds (VOCs), photo-products and oxygenated species, tracers, actinic flux, meteorological parameters, and aerosol composition and size distribution (Thompson et al., manuscript in preparation, 2021). This work focuses exclusively on the aerosol observations and also uses measurements of O_3, CO, pressure, temperature, water vapor, and GPS-derived aircraft location.

The aerosol size distribution instruments and their performance during ATom have been described in detail in several previous publications, which provide comprehensive documentation of the quality of the ATom aerosol dataset. Williamson et al. (2019) detail the function and performance of a multi-channel battery of condensation particle counters (NMASS: nucleation-mode aerosol size spectrometer) used to count and size particles with diameters (D_p) from ~3 to ~55 nm. Kupc et al. (2018) describe the calibration and performance of an ultra-high sensitivity aerosol spectrometer (UHSAS, Droplet Measurement Technologies, Longmont, CO, USA), an optical particle counter that measures the particle size distribution from ~60 nm (0.06 µm) to 1.0 µm. Brock et al. (2019) detail how these instruments are combined with a laser aerosol spectrometer (LAS, TSI Inc., St. Paul, MN, USA) to generate continuous, 1 s particle size distribution measurements from 3 nm to 4.8 µm, referred to as the aerosol microphysical properties (AMP) size distribution. Brock et al. (2019) also describe the sampling system, uncertainties, and data products associated with these dry particle size distribution measurements and show that data from these instruments are internally consistent and also agree with independently measured aerosol composition and extinction measurements within expected uncertainties.

Section 2.3 below describes in detail how dry size distributions and aerosol composition data from the in-cabin instruments are combined with data from an underwing cloud and aerosol spectrometer (CAS, Droplet Measurement

150 Techniques, Longmont, CO, USA; Baumgardner et al., 2001; Spanu et al., 2020). The CAS is a nearly open-path laser

optical particle counter that measures the size distribution of aerosol and cloud particles with diameters from 0.5–50 μm at

near-ambient conditions.

Aerosol composition was determined using two mass spectrometers and black and brown carbon measurements.

Froyd et al. (2019) provide a detailed description of how data from a single-particle laser ionization mass spectrometer

155 (PALMS; particle analysis by laser mass spectroscopy) are combined with particle size distributions to determine the size-

resolved composition and mixing state of particles with D_p from 0.14–4.8 μm. In addition, a high-resolution time-of-flight

aerosol mass spectrometer (HR-ToF-AMS, hereafter AMS for brevity, Aerodyne Inc., Billerica, USA; DeCarlo et al., 2006;

Canagaratna et al., 2007; Schroder et al., 2018; Hodzic et al., 2020), which provides bulk composition of particles with

geometric D_p from ~0.02 to ~0.7 μm, with detection efficiencies >50% between ~0.05 and ~0.5 μm (Guo et al., 2020),

160 collected data over ~46 s every minute, and reported with 1 s and 1 min. time resolutions (Jimenez et al., 2021). The AMS

can also provide size-dependent non-refractory composition information using particle time-of-flight measurement mode,

but in the free troposphere this often requires extensive time averaging which is impractical to apply during the vertical

profiles.

Measurements of refractory black carbon (BC) were provided by a single particle soot photometer (SP2; Gao et al.,

165 2007; Schwarz et al., 2010; Katich et al., 2018). This instrument uses laser-induced incandescence to measure the BC mass

within individual particles in the accumulation mode size range. BC mass concentration data, corrected to reflect

accumulation mode BC outside of the detection-range of the instrument, are reported on a 1 s time basis (with frequent null

detections at this rate at the concentrations found in ATom), while information on the size distribution of the BC and on the

thickness of non-refractory coatings on the BC particles can be obtained by accumulating data over longer time periods.

170 Brown carbon (BrC) absorption at wavelengths from 300–700 nm was determined by off-line analysis of aerosol

filter samples collected over times ranging from <5 minutes at low altitude to ~15 minutes at high altitude (Zeng et al.,

2020). A total of 1,074 filters from the ATom project, including 2–3 blanks per flight, were analyzed. Water extracts from

the filter were further filtered to remove BC, then introduced into a liquid waveguide where the spectral absorption was

measured with a spectrophotometer. The absorption of BrC by chromophores in the aqueous sample was then converted to

175 aerosol absorption.

We also use 1 s data from a precision open-path water vapor sensor (Podolske et al., 2003) with an uncertainty of

±5% and from the meteorological measurement system (Scott et al., 1990) of temperature measured within uncertainty of

±0.3 K and of pressure with an uncertainty of ±0.3 hPa, yielding an uncertainty in relative humidity with respect to water

(RH) that ranges from ± ~7% (of the value) in the warm, tropical marine boundary to ± ~6% (of the value) in the cold, dry

180 lower stratosphere. To identify stratospheric air, we use measurements of CO and O_3, which were measured using a

multipass optical absorption cell (McManus et al., 2005) and chemiluminescence (Ryerson et al., 1998), respectively.

Aerosol measurements can be contaminated by particles resuspended from the inlet walls due to hydrometeor

collisions (Murphy et al., 2004). Throughout this analysis, we use data that were obtained only in cloud-free air, as

determined by the absence of significant concentrations of droplet or precipitation-sized particles in the CAS measurements.

185 We include data that are within the CAS "haze" category as described in the broader ATom dataset (Wofsy et al., 2018),

which might have some contamination from cloud droplets. Excluding data from this category would remove substantial

quantities of the data within the MBL, which often dominate column-integrated optical properties. All concentration units

are reported at standard temperature and pressure (STP; 1013 hPa and 273.15 K); however, extensive optical properties such

as extinction and absorption coefficients are reported at ambient temperature and pressure conditions and, where indicated, at

190 ambient RH.

2.3 Determining the composition-dependent aerosol size distribution

Calculating ambient aerosol properties relies upon combining data from multiple sizing and compositional

instruments to develop a comprehensive description of the size-dependent composition and mixing state of the aerosol. From

this information the hygroscopic growth and refractive index, which are essential to estimating optical properties of the

195 hydrated aerosol, can be estimated. Figures 2 and 3 show how data from the four size distribution instruments are combined

with data from the four composition instruments and compositional and optical models to determine the ambient optical properties.

The PALMS instrument measures mass spectra of ion fragments from the laser-induced thermal desorption of individual aerosol particles (Thomson et al., 2000). Each mass spectrum is classified into one of several categories using

200   spectral signatures based on laboratory calibrations: sea salt, biomass burning, mixed sulfate/organic mixtures (which may also contain nitrate, ammonium, and other inorganic ions), soil dust, heavy fuel oil combustion, meteoritic material, alkali salts, elemental carbon (EC), and an unclassified fraction (Froyd et al., 2019). Because each individual particle is aerodynamically sized prior to laser ablation, each can be classified by both composition and size, and the number fraction of each compositional class can be determined for a given particle size range (Froyd et al., 2019). The size-resolved PALMS

205   composition data are converted from aerodynamic to geometric D_p by applying a particle density and shape for each class. However, the PALMS cannot directly measure a composition-based size distribution because it is limited by data rate, typically ~4 s^{-1}, and because it has size-dependent sampling biases. Instead, a statistical description of aerosol composition in specific size classes determined from PALMS can be combined with independently measured particle size distributions to provide a size distribution for each of the particle types (Froyd et al., 2019). For this analysis, the PALMS particle types

210   were aggregated over four size ranges (0.14–0.25 μm, 0.25–0.63 μm, 0.63–1.13 μm, and >1.13 μm); four bins provides a satisfactory tradeoff between number of bins, counting statistics per bin, and spatial resolution (Froyd et al., 2019). Within each of these size ranges, the different size particles contribute unevenly to the compositional statistics depending on their abundance and the efficiency of detection (Froyd et al., 2019). Depending on ambient concentrations, time averaging may be needed to achieve statistical significance. Once adequate compositional statistics are developed as described below, the

215   accumulated data in the four size ranges are mapped onto the independently measured particle size distributions from the AMP instruments (Fig. 3; Froyd et al., 2019; Murphy et al., 2020).

In the remote troposphere during ATom, the aerosol with $D_p \geq 0.14$ μm was composed of distinct particle types (with one of the types being internally mixed sulfate/organic). Thus, to calculate optical and hygroscopic properties, we do not assume a weighted internal mixture of the chemical components, but rather treat the total aerosol as an externally mixed

220 collection of independent size distributions, each composed of one PALMS compositional type mapped onto the particle size

distributions.

For particles with D_p <0.14 μm, for which the PALMS instrument provides limited statistics over the averaging

times used here, we assume the particles are composed of a non-refractory internal mixture with composition given by the

AMS instrument which provides submicron bulk composition measured over D_p ~0.05–0.5 um (Guo et al., 2020; Fig. 3).

225 Further, the AMS composition is applied to the sulfate/organic, biomass burning, EC, and unclassified particle types for the

0.14–0.25 μm PALMS size range, over which diameters the AMS samples with unity efficiency (Guo et al., 2020).

Throughout this work, we average all data to a 1-minute time base determined by the AMS reporting interval. The

1-minute data frequency we use translates into a vertical resolution of ~450 m given the typical ascent and descent rates in

the middle and lower troposphere, with somewhat better vertical resolution at altitudes >9 km during ascents as climb rates

230 dropped. As noted by Hodzic et al. (2020), in background conditions during ATom a substantial fraction of the AMS organic

aerosol (OA) concentrations were below detection limit, and included negative values. We substitute negative AMS values

with zeros when calculating optical or hygroscopic properties (Sect. 2.5).

The PALMS data presented here were accumulated over three-minute time periods and then interpolated to the

235 same one-minute time interval as the AMS data. However, if fewer than 5 particles were classified by the PALMS

instrument in each PALMS size range over the three-minute period, average compositional information based on much more

extensive spatial averaging was applied to that size range. If the time interval in question were in the MBL, typical PALMS

compositional statistics from the MBL were applied. Similarly, if the aircraft were in the lower stratosphere (as identified by

CO <100 ppbv and O_3 >100 ppbv or >300 ppbv in the southern or northern latitudes, respectively), in a BB plume (BB

240 particle number fractions >0.5 and aerosol mass >1 μg m^{-3}), or a dust plume (dust mass fraction >0.3), representative

compositional statistics from these air masses were applied to the PALMS size range in question.

For PALMS data with poor statistics (<5 particles in a PALMS size range) in the free troposphere (FT), regionally

averaged particle composition statistics were applied. This situation most often applied to particles with D_p >1.13 μm, which

have very low number concentrations. These regionally averaged statistics were separately calculated and applied depending

245   on whether the DC-8 was over the Pacific or Atlantic Ocean, and whether it was in Antarctic/Southern Ocean, southern

midlatitude, tropical, northern midlatitude, or Arctic air masses. The latitudinal boundaries of these air mass types is

provided in the Supplemental Materials (Table S1). These same air mass classifications serve as a way to organize the final

data products that are the objective of this effort (Sect. 3.3).

The aerosol sampling inlet on the DC-8 aircraft excludes most particles with ambient D_p >4.8 µm at low altitude,

250   with the 50% passing efficiency falling to ~3.2 µm at high altitude (McNaughton et al., 2007; Brock et al., 2019). In

addition, the LAS optical particle counter, which measures the size distribution of the coarse mode using a red laser, suffers

from sizing ambiguities in the size range from ~1 to ~2 µm due to Mie oscillations in the scattering cross section. The LAS

also has poor coarse-mode counting statistics due to a sample flow rate of ~1 cm^{3}s^{-1}. For these reasons, we use data from the

under-wing CAS probe, which has an optically defined sample flow rate of ~50 cm^{3}s^{-1} (Spanu et al., 2020), for particles with

255   D_p >1.01 µm. The CAS suffers from similar sizing ambiguities as does the LAS. However, a data processing scheme similar

to the technique described by Walser et al. (2017) combined with a Monte Carlo method (Spanu et al., manuscript in

preparation, 2021) is used to retrieve a size distribution, with uncertainties, that minimizes these biases. Because the CAS

measures at ambient RH, the data are corrected for water uptake using hygroscopic growth estimated from κ-Köhler theory

(Petters and Kreidenweis, 2007), based on the composition of the PALMS instrument in its largest size range (1.14 to ~4.8

260   µm; Fig. 3; Table 2). The "dried" CAS data are combined with the AMP measurements to provide continuous dry size

distributions over D_p from 3 nm to 50 µm.

BC particles are treated separately from the rest of the aerosol measured during ATom. The SP2 instrument reports

the mass of refractory BC cores with spherical volume-equivalent D_p from 90–500 nm as a function of time. Statistics

regarding the size distribution of the BC cores, as well as estimates of the average coating thickness on them, can be

265   obtained with extensive averaging at the BC concentrations found in ATom (outside of pollution layers and biomass burning

plumes). The size distribution and coating thickness of BC particles were averaged over the same air mass regions as were

the PALMS data when counting statistics were insufficient (Fig. S1). As described in Sect. 2.7.1, the averaged, coated size

distributions from the SP2 measurements are used to estimate the absorption and other optical properties. However, the BC

size distribution is not combined with the other size distribution measurements, which are assumed to represent the purely

270   scattering aerosol. In other words, we assume two independent types of size distributions: 1) the composition-dependent size

distributions of biomass burning, derived from the AMS, PALMS, and size distribution measurements that together describe

all non-absorbing aerosol components, and 2) the size distributions of coated BC particles from the SP2 instrument that are

averaged over air mass types and used to calculate aerosol absorption as described in section 2.7.1. (Note that coated BC

particles would also be measured by the size distribution instruments, but these are generally a few percent of the total

275   number concentration and represent a minor double-counting error.)

Note that the PALMS instrument reports an "EC" (or "soot") compositional class, which is closely related to the BC

particles measured by the SP2 instrument. However, because the PALMS distinguishes only a small (and uncertain) fraction

of all particles containing EC (Murphy et al., 2006), we simply assign all "EC" particles detected by PALMS to the non-

absorbing "sulfate/organic" class for the purpose of calculating aerosol optical and hygroscopic properties. Absorbing BC

280   particles are assumed to be adequately represented by the more quantitative SP2 measurements alone.

2.4 Modal fits to dry size distributions

In global models, aerosol optical properties depend upon an accurate description of the size-resolved composition of

dry particles, which is often described by lognormal parameters that represent different aerosol modes. To compare with

these representations, lognormal fits were made to each mode (nucleation, Aitken, accumulation, and coarse) of the dry size

285   distributions measured during ATom. The lognormal equation used is

$$\frac{dX}{dlog_{10}D_p} = \frac{Xln(10)}{\sqrt{2\pi}ln(\sigma_g)}exp\left\{-0.5\left(\frac{ln(D_p/D_{g,x})}{ln(\sigma_g)}\right)^2\right\}, \qquad (1)$$

where the three fitted parameters are X, which represents number, surface, or volume, the geometric standard deviation σ_g,

and the geometric mean diameter, $D_{g,x}$. These fits were made to the volume-weighted size distribution for the coarse (D_p>1

μm) and accumulation (0.08> $D_p \leq$ 1 μm) modes, and to the number distribution for the Aitken (0.012> $D_p \leq$ 0.08 μm) and

290 nucleation (0.03≥ D_p ≤0.012 µm) modes. The fits began with the coarse mode and proceeded toward the nucleation mode.

Once fitted, each larger mode was subtracted from the size distribution and the fit of the next smallest mode was made from

the residual size distribution. This fitting method is described in more detail in the Supplemental Materials. All descriptions

of aerosol properties are based on the measured, rather than fitted, size distributions, unless otherwise noted.

2.5 Calculating ambient size distributions

295   To determine the growth of the dry particles to ambient diameter at the measured ambient water vapor saturation

ratio (=RH/100), the hygroscopicity must be estimated for each of the aerosol types. The hygroscopicity of the particles is

described by κ using κ-Köhler theory (Petters and Kreidenweis, 2007). In this parameterization, the wet particle diameter

D_{drop} can be determined at a given water vapor saturation ratio $S(D_{drop})$ as

$$S(D_{drop}) = \frac{D_{drop}^3 - D_p^3}{D_{drop}^3 - D_p^3(1-k)} exp\left(\frac{4\sigma_{drop}M_w}{RT\rho_w D_{drop}}\right), \tag{2}$$

300 where D_p is the diameter of the dry particle, σ_{drop} is the surface tension of the droplet (0.072 J m^{-2}), R is the universal gas

constant (8.314 J mol^{-1}), T is the ambient air temperature (K), and ρ_w and M_w are the density and molecular weight of water

(1000 kg m^{-3} and 0.018 kg mol^{-1}, respectively). For particles whose non-refractory composition is described by the AMS (all

particles with D_p<0.14 µm and the sulfate/organic, biomass burning, meteoritic, EC and unclassified fractions between 0.14

and 0.25 µm), an algebraic inorganic electrolyte composition model (Zaveri, 2005) was used to calculate the concentrations

305 of ammonium sulfate, ammonium bisulfate, letovicite, sulfuric acid, ammonium nitrate, ammonium chloride, nitric acid, and

hydrochloric acid from the AMS measurements of sulfate, nitrate, ammonium, and chloride. For this calculation, negative

AMS values (which can occur due to background air signal subtraction; Jimenez et al., 2021) were set to zero. The volume-

weighted κ from these electrolytic species (Table 2) was used to estimate the inorganic κ for each data point. The κ of the

OA was estimated using the ratio of O/C reported by the AMS as

310                      $\kappa_{OA} = 0.19\times(O/C)–0.0048,$ \qquad\qquad (3)

following Rickards et al. (2013). The κ_{OA} values are smoothed with a running 10-point binomial smoothing algorithm to

reduce noise. The project-wide average organic κ_{OA} from this method was 0.18±0.03. An analysis of the relationship between

κ_{OA} and the O/C ratio (Nakao, 2017) found that volatility and solubility are also key parameters in determining κ_{OA}, but we

lack the additional information on such properties needed to provide a revised estimate. The Zaveri/κ-Köhler approach was

315 used successfully to simulate observed aerosol hygroscopic growth over a wide range of aerosol compositions in the

southeastern United States (Brock et al., 2016a). The value of κ was estimated as a volume-weighted sum of the κ values of

the non-refractory organic and inorganic components from the AMS measurements and the inorganic composition model,

using the values listed in Table 2. The overall project-mean value of κ from the AMS measurements was 0.53±0.19

For particles with D_p >0.25 μm in the PALMS sulfate/organic, BB, meteoritic, EC and unclassified compositional

320 classes, κ was estimated using the PALMS-measured organic mass fraction, F_{org},

$$\kappa = (1-F_{org}) \times 0.483 + F_{org} \times 0.17, \tag{4}$$

based on laboratory calibrations, assuming particles were composed only of sulfate and organic material (Froyd et al., 2019).

For a pure organic aerosol (F_{org}=1), this yields κ_{org} =0.17, close to the AMS project-wide value of κ_{org}=0.18 from Eq. 3. The

project-wide mean value of κ from Eq. 4 for particles with D_p>0.25 μm was 0.36±0.05.

325 Applying the values of κ listed in Table 2, the *RH* determined from measured static air temperature and water vapor

mixing ratios, and Eq. 2, the dry size distributions for sea salt, BB, sulfate/organic, soil dust, heavy fuel oil combustion,

meteoritic material, and alkali salts were used to calculate ambient size distributions for each composition class. The

contribution of water was calculated from the difference between the wet and dry size distributions for each composition

class.

330 The CAS instrument measures at ambient conditions, so it should not be necessary to "re-grow" the dry size

distributions from this instrument, which were calculated using an iterative technique that involves Mie-calculated

instrument response, κ values, and refractive index to determine ambient sizes (Spanu et al., manuscript in preparation).

However, we wish to develop an internally self-consistent dataset in which the compositionally based dry size distributions

and the size-dependent values of κ for each of these aerosols can be used to directly calculate the ambient size distribution at

335 the ambient RH. For this reason, we use the dry size distributions calculated from the CAS algorithm for D_p >1.01 μm,

append them to the in-cabin dry size distribution measurements, apply the compositional information from the largest

PALMS size class (1.13<D_p ≤ 4.8 μm) to estimate a κ value for each aerosol type, and then calculate the ambient size distribution.

2.6 Calculating cloud condensation nuclei

340   The concentrations of cloud condensation nuclei (CCN) at several fixed supersaturations were calculated based on the observed dry size distributions and the composition determined from the AMS and the inorganic composition model (Zaveri et al., 2005). To calculate the critical wet diameter, D_{crit}, Eq. 2 was iteratively solved with different D_{drop} using a fixed D_p and a fixed κ determined from the measurements as described in Sect. 2.5 until the maximum supersaturation S_{max} was found. This process was repeated for different D_p until S_{max} matched the supersaturation for which the CCN

345   concentration was being calculated, giving $D_{crit,dry}$, the dry D_p that yielded D_{crit} for a given κ and S_{max}. The number size distribution was then integrated across all $D_p{\geq}D_{crit,dry}$, yielding the calculated CCN concentration for that minute of flight. For ATom, CCN concentrations were calculated for fixed supersaturations of 0.05%, 0.1%, 0.2%, 0.5%, and 1.0%.

2.7 Calculating dry and ambient optical properties

2.7.1 Extensive optical parameters

350   Scattering was calculated for each of the composition-based size distributions independently as

$$\sigma_{s,i}(\lambda) = \int_{3\,nm}^{50\,\mu m} \frac{\pi}{4} D_p^2 \alpha_{s,i}(D_p, n_i, \lambda) N_i(D_p) dlog_{10}(D_p), \tag{5}$$

where $\sigma_{s,i}$ is the scattering caused by composition i (Sect. 2.4.1), $\alpha_{s,i}$ is the scattering efficiency at wavelength λ calculated from Mie theory using real refractive index n_i (Table 2), and N_i is the number concentration of particles of composition i within the logarithmic size interval $dlog_{10}(D_p)$. All particle types were treated as spherical in shape for optical calculations.

355   Scattering was calculated for the wavelengths of 340, 380, 405, 440, 532, 550, 670, 870, 940, and 1020 nm, which match common wavelengths for the AERONET sunphotometers and satellite measurements of AOD. The refractive indices in Table 2 are not adjusted for wavelength; this is a small potential bias in the context of other assumptions and approximations in the calculation. The refractive indices for the sulfate/organic, biomass burning, meteoritic, and EC compositional classes

are calculated from the volume-weighted components from the inorganic compositional model and the organic mass.

360   Additionally, the refractive indices for the hydrated ambient aerosol are adjusted on a volume-weighted basis for the water

content. Total scattering is the sum of the scattering from the individual composition-based size distributions ($\sigma_{s,tot}(\lambda) =$

$\sum_i \sigma_{s,i}(\lambda)$).

        Scattering coefficients were also calculated for the particle size distributions at fixed RH values of 70, 80, and 85%

at 532 nm wavelength. These values are used to fit a parametric curve describing *f(RH)*, the RH dependence of scattering, as

365   described in Sect. 2.7.2.

        Absorption due to BC was calculated using measurements of BC core size and coating thickness from the SP2

instrument, averaged over the air mass type. Coating thickness could be determined only from the subset of cores with BC

mass between ~2.5 and 6 fg (~140–330 nm volume equivalent diameter), but this average coating thickness was applied to

all BC cores measured (Gao et al., 2007). The coated size distributions were used to calculate mass absorption cross-sections

370   (MACs; absorption per unit mass concentration) at the same wavelengths of 340, 380, 405, 440, 532, 550, 670, 870, 940, and

1020 nm for each air mass type via core-shell Mie theory (Bohren and Huffman), assuming that the refractive index of the

BC (Moteki et al., 2010; Table 2) remains constant across these wavelengths (Bond et al., 2013). The calculated regional-

average MACs were then multiplied by the 60-s-averaged BC mass measured within each respective region to estimate

absorption due to the BC ($\sigma_{a,BC}$) on a 60-s time base. We assume that hygroscopic growth on coated BC particles does not

375   appreciably change the absorption coefficient through additional lensing effects, since substantial coatings on the aged BC

particles already existed. Absorption due to dust particles was not calculated; such absorption is expected to be significant in

the ATom dataset only in Saharan dust plumes.

        In addition to broad-spectrum absorption by BC, certain organic species absorb light in blue and near-UV

wavelengths; these compounds are referred to as brown carbon (BrC). Most of the BrC in the remote atmosphere is believed

380   to originate from biomass burning (e.g., Washenfelder et al., 2015). Absorption due to BrC may change with time from

emission due to photo-bleaching of chromophores or to secondary production of absorbing organic species (e.g., Forrister et

al., 2015; Liu et al., 2020). Absorption from 300–700 nm wavelength due to water-soluble (WS) BrC was measured during

deployments 2–4 of the ATom project (Zeng et al., 2020). These measurements were made using aqueous extracts from

Teflon filters collected over 5–15 minute periods. Because of these long sampling periods, it is difficult to directly combine

385   the BrC measurements with the 60s data used in this analysis. However, we can take advantage of the observed correlations

between WS BrC absorption and BC mass and between WS BrC absorption and the PALMS biomass burning mass

(Supplemental Materials in Zeng et al., 2020) to roughly estimate the WS BrC at 365 nm at 60-s frequency. This proxy WS

BrC is calculated from a multivariate linear regression between these parameters and is then multiplied by a factor of 2 to

approximately account for unmeasured BrC that is extractable in organic solvents, and another factor of 2 to convert from

390   bulk liquid absorption to aerosol absorption (Zeng et al., 2020). The final proxy relationship is

$$\sigma_{a,BrC}(365nm) = 4(a_1 M_{BB} + a_2 M_{BC}), \tag{6}$$

where a_1 and a_2 are parameters from the multivariate linear regressions from ATom 3–4, and M_{BB} and M_{BC} are the mass

concentrations of the PALMS biomass burning particles and the SP2 BC, respectively. Only values from ATom 3 and 4

were used for Eq. 6 because most BrC measurements during ATom-2 derived from two regions of burning in Africa and

395   South America, while during ATom-3 and -4, more dilute smoke from a range of geographic regions was sampled. The

values of a_1 and a_2, were 0.07 ± 0.06 and 5.4 ± 1.1 m^2g^{-1}, respectively. A two-sided linear regression between this proxy BrC

and the measured values yielded a slope of 0.68 ± 0.06 and $r^2=0.40$.

Given the modest ability of the proxy BrC absorption to predict the measured values, as well as the uncertainty in

accounting for organic-soluble BrC and in the conversion from liquid to aerosol absorption, this $\sigma_{a,BrC}$ is probably accurate to

400   within only a factor of ~3. The absorption coefficients due to BrC at the wavelengths used to calculate scattering and

extinction were estimated using an absorption Ångström exponent value of 5 (Zeng et al., 2020). The absorption due to BrC

calculated in this way was added to the BC absorption and to total scattering calculated as described above to provide total

aerosol extinction: $\sigma_e(\lambda) = \sigma_{s,tot}(\lambda) + \sigma_{a,BC}(\lambda) + \sigma_{a,BrC}(\lambda)$.

During ATom-4, the SOAP (spectrometers for optical aerosol properties) instrument measured dry aerosol

405   extinction at a wavelength of 532 nm using cavity ringdown spectrometry (Langridge et al., 2011). For comparison with this

direct extinction measurement, dry extinction was calculated for a truncated size distribution to match the SOAP instrument,

which operated behind a 2 μm-aerodynamic-diameter impactor. This calculated extinction agreed within experimental

uncertainties with the SOAP extinction (Fig. 4a), with a slope of 1.04 and a Pearson's regression coefficient (r^2) of 0.96.

Similarly, the absorption calculated from the SP2 measurements as described in Sect. 2.7.1 agreed well with the SOAP

410 photoacoustic absorption spectrometer (Lack et al., 2012) during ATom-4 when the absorption signal was greater than the

SOAP noise level of ~2×10^{-6} m^{-1} (Fig. 4b), with a slope of 0.95 and r^2=0.84. These comparisons between the calculations of

extinction based on aerosol composition, size distribution, refractive index, and BC mass and coating thickness, and

independent, direct measurements of extinction and absorption provide confidence that the calculated optical properties

represent the bulk submicron aerosol properties in the atmosphere with good fidelity.

415 **2.7.2 Intensive optical properties**

      Intensive aerosol properties are those that do not vary with abundance. All intensive optical properties were

calculated at wavelengths of 340, 380, 405, 440, 532, 550, 670, 870, 940, and 1020 nm. Single scatter albedo ω_0 is the ratio

of scattering to total extinction ($\sigma_{s,tot}/\sigma_e$). The value of ω_0 was calculated for both the total dry size distributions as well as

those at ambient RH. For the ATom dataset, the absorbing component is calculated from regionally averaged MAC values

420 multiplied by the 60 s BC mass concentrations, and from the proxy $\sigma_{a,BrC}(\lambda)$, as described in Sect. 2.7.1. We do not attempt

to model absorption by adjusting the imaginary refractive index of the different components of the composition-resolved size

distributions because this would be a severely underconstrained problem.

      Mass extinction efficiency is the ratio of extinction to aerosol mass concentration. This size-dependent parameter is

calculated from the dry size distributions using the total dry extinction coefficient σ_e and the total aerosol mass, which is the

425 sum of the aerosol density for each composition component (Table 2) multiplied by the particle volume from the integrated

size distribution for that component.

      Phase function $P(\theta)$ is the normalized angular distribution of light intensity scattered by an aerosol in angle θ

relative to the incident radiation. For spherical (Mie) scatterers, it is defined as

$$P_i(\theta) = \frac{I(\theta)}{\int_0^\pi I(\theta) \sin\theta d\theta}, \tag{7}$$

430 where I is the intensity of the scattered light from an aerosol of composition class i. The asymmetry parameter g is a

simplified description of the phase function that is often used in radiative transfer approximations such as the Henyey-

Greenstein phase function or the delta-Eddington approach, which are then applied within global-scale models. The

asymmetry parameter for an aerosol of composition i is defined as

$$g_i = \frac{1}{2} \int_0^\pi \cos\theta P_i(\theta) \sin\theta d\theta. \tag{8}$$

435 The value of g_i will range from -1 (purely backward-scattered light) to +1 (purely forward-scattered light). Typical

values for accumulation-mode dominated size distributions for mid-visible wavelengths are ~0.4–0.6, with larger values

possible for size distributions with a substantial coarse fraction (e.g., Andrews et al., 2006). We calculate the total aerosol g

for both dry and ambient RH conditions from an extinction-weighted sum of the g_i from each composition-based size

distribution.

440 The fine mode fraction (η) is the fraction of the total extinction that is attributable to the fine mode (e.g., Anderson

et al., 2005). This is a parameter that can be retrieved from remote sensing measurements and that apportions the light

extinction between the fine (accumulation) mode, whose particles are mostly produced from combustion and secondary

processes, and the coarse mode, whose particles are mostly generated by mechanical processes. Because some of the coarse-

mode particles extend into the submicron size range (and vice versa), we use the modal fits to the composition-based size

445 distributions to calculate η. The refractive index of the coarse and fine modes used to calculate η is calculated from the

volume-weighted mean of each composition class in the size range of the mode.

The ratio of scattering at a given RH to that at dry conditions, or $f(RH)$, can be parameterized simply using a

physically based function,

$$f(\lambda, RH) \equiv \frac{\sigma_{s,tot}(\lambda, RH)}{\sigma_{s,tot}(\lambda, RH=dry)} \simeq 1 + \kappa_{ext} \frac{RH}{100-RH}, \tag{9}$$

450 where κ_{ext} is a fitted parameter that is related to, but not identical to, the κ in κ-Köhler theory (Brock et al., 2016a). Because

the dry size distributions are assumed to be measured at RH=0%, no correction to Eq. 9 to account for residual water (Titos

et al., 2016; Kuang et al., 2017; Burgos et al., 2020) is applied. The value of κ_{ext} was calculated for each 60s time data

interval by least-squares fitting of Eq. 9 to the scattering values calculated at the dry condition and at RH values of 70, 80,

and 85%, for each of the 10 wavelengths considered. Separately, the value of *f(RH)* was calculated for RH=85% for

455   comparison with literature values (Burgos et al., 2020).

    The Ångström exponent describes the power law relationship between extinction, scattering, or absorption and the

wavelength of incident light:

$$\frac{\sigma_x}{\sigma_{x,0}} = \left(\frac{\lambda}{\lambda_0}\right)^{-\gamma_x}, \tag{10}$$

where x represents extinction (e), scattering (s), or absorption (a) and λ is the wavelength of incident light, γ is the Ångström

460   exponent, and the naught subscript indicates a reference wavelength. The value of γ_e is determined by making a least-squares

fit to the calculated values of σ_e at wavelengths of 340, 380, 405, 440, 532, 550, 670, 870, 940, and 1020 nm. The value of γ_a

for $\sigma_{a,BrC}$ is assumed to be 5. For $\sigma_{a,BC}$, γ_a is calculated from regionally averaged BC size distributions using core-shell Mie

theory (Sect. 2.7.1). Thus an absorption Ångström exponent is provided on only a regionally averaged basis, rather than at

the 60-s resolution for which γ_s is calculated.

465   **2.8 Calculating aerosol optical depth**

    During ATom the DC-8 executed repeated en-route ascents and descents between ~0.16 and ~12 km approximately

every 30–60 minutes. By integrating ambient extinction or absorption vertically during each ascent or descent, extinction

AOD and absorption AOD (AAOD) can be calculated. Because ambient extinction is calculated for each composition class,

it is possible to determine the portion of AOD attributable to each of these classes, along with the associated water. This

470   provides a valuable dataset with which to apportion AOD amongst different aerosol types, and can be used to compare with

model representations of AOD and with assumptions regarding aerosol types used in remote sensing retrieval algorithms.

    To adequately represent atmospheric AOD and AAOD, each integrated profile should contain representative

measurements in the MBL, where sea-salt aerosol often dominates total AOD. The profiles should also contain any optically

significant layers, such as biomass burning and dust plumes, that may be present. To ensure that the profiles represent

475 atmospheric AOD, the following rules were used: 1) data were integrated over 1 km thick layers, 2) the profile must have

extended from the bottom 1 km layer to at least 8 km in altitude, 3) the bottom two layers (0–2 km) both must have

contained valid extinction data, 4) no more than 2 layers above the required bottom 2 layers could have been discarded due

to cloud screening, and 5) data were interpolated across up to two such discarded layers. There are typically one or two 60-s

average data points within each layer for each profile.

480 Atmospheric AOD and AAOD were calculated as

$$AOD_\lambda = \sum_{i=0}^{N} \overline{\sigma_{x,\lambda,i}} \Delta z, \tag{11}$$

where i represents each 1-km thick layer Δz beginning at altitude $z=0$ km, and $\overline{\sigma_{x,\lambda,i}}$ is the ambient extinction (for AOD) or

absorption (for AAOD) coefficient for wavelength λ averaged from the 60-s data within the layer.

3. Results

485 ### 3.1 Aerosol extinction

Aerosol extinction was calculated for both the dry and ambient RH conditions, at STP as well as at ambient

pressure and temperature. The difference between the ambient RH and dry extinction values provides the extinction due to

H_2O. The spatial pattern of ambient total extinction and that due to the aerosol components that dominate AOD–biomass

burning, sulfate/organic mixtures, sea salt, dust, and H_2O–are shown in Fig. 5. This figure shows the comprehensive

490 coverage in altitude and latitude of the ATom flights and provides an overview of the spatial patterns of the contribution of

different aerosol species to AOD. Total ambient extinction in the remote marine atmosphere (Fig. 5a; b) is dominated by sea

salt and associated water in the MBL (Fig. 5g; h; k; l), with several notable exceptions. Biomass burning aerosol over the

northern subtropical Atlantic, and to a lesser extent over the southern subtropical Atlantic and the tropical and northern

midlatitude Pacific, at altitudes <4 km, is an important contributor to dry extinction (Fig. 5c; d; Schill et al., 2020). In

495 general, the Northern Hemisphere has more biomass burning extinction than the southern. Contributions to extinction from

sulfate/organic particles of mostly secondary origin (Fig. 5 e; f; Hodzic et al., 2020) are substantially higher in the Northern

than the Southern Hemisphere, especially over the Pacific, due to higher biogenic and anthropogenic emissions in the more

populated Northern Hemisphere.

Extinction due to dust is important in the tropics and subtropics of the Atlantic Ocean due mostly to emissions from

500   the Sahara Desert (Fig. 5i; j). There are also significant contributions to extinction from dust in the mid-latitudes of the

Atlantic and in the free troposphere (FT) of the northern Pacific due to dust emitted from Asia and the Sahara (Froyd et al.,

submitted manuscript, 2021). There is very little extinction from dust in the Southern Hemisphere at altitudes >2 km, in

sharp contrast with the Northern Hemisphere.

3.2 AOD and comparison with AERONET

505   The ambient extinction measured during each profile (Fig. 5) was vertically integrated as described in Sect. 2.8 to

calculate AOD. Several of these profiles were near Aerosol Robotic Network (AERONET) sites. AERONET is an affiliation

of ground-based remote sensing sites that use consistent methodologies, calibrations, and instrumentation to make sun

photometer measurements of AOD and, in cases of high atmospheric turbidity, aerosol optical and microphysical properties

(Holben et al., 1998; 2006). These measurements provide an opportunity to compare AOD calculated through the complex

510   process outlined in Figs. 2 and 3 with directly measured values. Individual profiles were selected for comparison with

AERONET if 1) the location of the aircraft at the midpoint in time between the start and end of the profile was within 300

km of the AERONET site, and 2) if the midpoint time was within ±4 hours of an AERONET data record. An exception was

made for the Macquarie Island site, as it was the only AERONET site with data in the Southern Ocean. Macquarie Island

was 421–601 km from the midpoint of the nearest three DC-8 profiles. For comparisons of AOD with the AERONET site at

515   the Mauna Loa Observatory, which lies at 3.4 km altitude, the DC-8 profile was integrated upward beginning with the 3–4

km altitude bin. Version 3 Level 2.0 AERONET data were used for all comparisons, and the AOD at 532 nm was

interpolated from observations at 500 and 675 nm using the Ångström equation (Eq. 10).

A linear regression between the calculated and measured AOD (Fig. 6) produces a slope of 0.96 with r^2=0.69.
While many of the individual data points do not have error bars that overlap with the 1:1 line, the error bars account for only
520 instrumental uncertainty, not atmospheric variability. Given that the average distance between the AERONET sites,
excluding Macquarie Island, and the midpoint of the DC-8 profiles was 161 km, the agreement is surprisingly good, and
indicates that the methodology to calculate ambient aerosol optical properties is sound.

   Figure 7 shows the calculated AOD for each profile with valid extinction data meeting the criteria in Sect. 2.8, a
total of 639 profiles. While there is great variability in AOD from these individual profiles, general patterns are evident.
525 First, the Northern Hemisphere midlatitudes and polar regions have substantially higher AOD than the same latitudes in the
Southern Hemisphere, often by a factor of 2 or more. This difference reflects the much higher continental emissions of
aerosols and precursors in the northern hemisphere. Second, the tropical and subtropical Atlantic has the highest AOD values
found during the ATom flights due to Saharan dust and strong emissions from African biomass burning. Finally, low values
of AOD, of order 0.01, are frequently found over the Southern Ocean and near the Antarctic Peninsula. In the absence of
530 high winds to produce abundant sea-salt aerosol, these regions of the troposphere have the least influence from
anthropogenic and continental sources, and thus the least aerosol extinction. The contributions of different aerosol types to
extinction profiles in different regions of the atmosphere are examined in more detail in Sect. 3.3.1.

3.3 Aerosol characteristics in different air masses

   To summarize and present the data, aerosol characteristics were averaged over the same spatial regions over which
535 PALMS free tropospheric compositions were averaged. These regions are schematically represented in Fig. 8, and include
the tropics, the midlatitude and polar regions for the northern and southern hemisphere and for the Pacific and Atlantic ocean
basins, and the northern and southern high latitude stratosphere. The precise latitudinal definitions of these regions were
based on analysis of the air mass characteristics encountered, and varied with each ATom deployment as indicated in Table
S1 in the Supplemental Materials. The top of the MBL in each profile was identified by manually inspecting the data for a
540 sharp gradient in gas-phase tracers such as O_3, NO_2, CO and H_2O, and in particle number, with relatively homogeneous

mixing ratios below this altitude. The top of the MBL was often quite ambiguous, particularly over colder waters where thorough atmospheric mixing may not take place. Different definitions of the MBL height are unlikely to substantively change most conclusions given the relatively coarse temporal resolution of the averaged data (~60 s) and the associated vertical resolution (~450 m). However, if aerosols with MBL characteristics (e.g., high concentrations of sea-salt particles)

545   are present above the identified top of MBL, they may skew average compositions for the FT.

The stratosphere was defined as O_3 >100 ppbv and CO <100 ppbv in the Northern Hemisphere and O_3 >300 ppbv and CO <100 ppbv in the Southern Hemisphere. These definitions were chosen based on the occurrence of a mode of nearly pure sulfuric acid particles and particles with a meteoritic core and sulfuric acid coating, indicating that the aircraft was sampling predominantly stratospheric particles (Murphy et al., 2020). The maximum altitude reached by the DC-8 was 13.2

550   km, and much of the stratospheric air was sampled when the tropopause heights were low in the winter hemisphere or in tropopause folds. The maximum O_3 observed, 957 ppbv, was measured at an altitude of 11.3 km at 68° N latitude when CO was 22.2 ppbv.

Regardless of altitude or region, samples were classified as being in a biomass burning plume when the number fraction of particles classified by PALMS as "biomass burning" by their potassium- and carbon-rich ion signatures (Hudson

555   et al., 2004; Schill et al., 2020) was >0.5 and total mass concentrations were >1 μg m^{-3}. Similarly, dust cases were identified when the number fraction of PALMS "mineral dust" particles was >0.3.

3.3.1 Extinction profiles

The contribution of different aerosol components to extinction varies significantly with altitude and air mass type. In Fig. 9 we present vertical profiles, averaged in 1-km bins, of the average contribution to extinction for the different

560   aerosol types, for all of the ATom deployments. These profiles include all non-cloudy data within the geographic region, including data taken in the MBL, in dust and BB plumes, and in the stratosphere. Sea salt in the MBL and associated waterdominates the extinction in most of the regions. However, there are notable exceptions. Over the Arctic (Fig. 9a), there are significant contributions from biomass burning and sulfate/organic particles, and associated water, declining with increasing altitude. Two of the ATom deployments took place in winter and spring, when northern hemisphere pollution

565 substantially affects the Arctic troposphere. The vertical profiles of extinction are consistent with the phenomenon of

chronic, background "Arctic haze" (Brock et al., 2011). In sharp contrast, the Antarctic/Southern Ocean profiles (Fig. 9b)

shows the dominance of sea salt and water, with minor contributions to extinction from biomass burning layers encountered

in the upper troposphere.

In the Pacific northern midlatitudes (Fig. 9c), biomass burning and sulfate/organic particles also contribute

570 significantly to extinction, and dominate above the MBL. These aerosol types are associated with plumes of pollution and

biomass burning from Asia. Dust contributes as well, but to a lesser extent. Fewer such layers were encountered over the

Atlantic at northern midlatitudes (Fig. 9d). Over the tropical and subtropical Atlantic (Fig. 9f), there is a significant

contribution from Saharan dust in the lower troposphere along with biomass burning, sulfate/organic particles, sea salt, and

absorption from BC. In contrast, the Pacific tropical lower troposphere (Fig. 9f) shows the dominance of sea salt and lesser

575 contributions from other components, similar to the Pacific and Atlantic southern midlatitudes (Figs. 9g,h).

Extinction in air classified as being in the MBL, in dust plumes (Fig. 10b) or in biomass burning plumes (Fig. 10c)

may also be attributed to specific aerosol components using the ATom dataset. Unsurprisingly, sea salt and associated water

dominate extinction in the MBL, followed by sulfate/organic mixtures, biomass burning aerosol, and dust. In dust plumes,

mineral dust particles dominate, followed by water, sulfate/organic particles, and BB particles. In biomass burning plumes,

580 particles containing biomass burning material dominate extinction, while sulfate/organic particles and water also contribute

substantially to extinction. Absorption from coated BC is also a significant contributor to the extinction budget of these

plumes.

3.3.2 Size-dependent composition

The PALMS single-particle mass spectrometer measures the composition and size of individual particles, which can

585 then be mapped to high-resolution particle size distributions to provide a representation of the composition-based size

distribution. Since many global models carry only the mass of different aerosol species and then prescribe their size

distribution with modal or sectional representations (e.g., Chin et al., 2002; Liu et al., 2016; Mann et al., 2010), the high-

resolution observations from ATom provide an important point of comparison. Aerosol-radiation and aerosol-cloud

interactions flow directly from the size of the particles and their optical and hygroscopic properties; thus it is essential that

590 models predict the right aerosol properties for the right reasons. In this section we present the average composition-

dependent size distribution of the aerosol in the different air mass types, which is useful for evaluating how different

compositions influence optical properties.

Two distinct volume (mass) modes are present in all air mass types; an accumulation mode between 0.1 and ~0.8

μm and a coarse mode at larger sizes (Fig. 11). Small peaks between ~0.6 and 2 μm (e.g., Fig. 11a) are likely due to

595 ambiguous instrument response at particle sizes near the wavelength of the lasers, and to overlaps between the underwing

CAS instrument and the in-cabin LAS instrument. Most of the other fine structure in the shape of these modes is due to

averaging together different size distributions. These average size distributions do not properly represent the aerosol's modal

characteristics. For example, averaging size distributions with two peaks might produce a mean distribution with an

excessively broad, flat mode that does not accurately describe the characteristics of either—or any—atmospheric size

600 distribution. However, these average size distributions usefully describe the contributions of different particle types to the

different modes. In Section 3.3.3, we use modal representations of the measured size distributions to more accurately

describe the shape of the aerosol size distributions and their statistics in different air mass types.

The composition-based size distributions with regional labels (i.e., the left two columns) are from the FT only and

exclude data from BB and dust plumes and stratospheric intrusions. Size distributions from the MBL, stratosphere, and BB

605 and dust plumes (right column) are not regionally separated; e.g., Fig. 11c is an average of all MBL size distributions in all

regions.

Water is the single most dominant component in all of the regionally averaged size distributions (left two columns).

In the Pacific and Atlantic northern midlatitudes (Figs. 11d, e) and the Atlantic tropics (Fig. 11h), the dry volume (ignoring

water) associated with the coarse mode is substantially larger than that of the accumulation mode, primarily due to the

610 contribution of mineral dust to the coarse mode. In the Arctic (Fig. 11a), dust is a major fraction of the dry coarse mode, but

the accumulation mode is larger due mostly to the sulfate/organic particles characteristic of Arctic haze (e.g., Brock et al.,

2011). In the tropical Pacific, southern midlatitude Pacific and Atlantic, and Antarctic/Southern Ocean, which are more

remote from continental sources (Fig. 11b, g, j, k), sea salt dominates the coarse mode of the FT when averaged over the

region, while sulfate/organic particles contribute most to the accumulation mode. Biomass burning particles are substantial

615   portions of the dry accumulation mode in all regions except the Antarctic/Southern Ocean (Fig. 11b), and to a lesser extent

over the South Pacific (Fig. 11g). The biomass burning particles are found mostly in the upper end of the accumulation mode

volume, consistent with the larger diameters typically found near wildfire sources (Radke et al., 1977) compared to

secondary particles from natural and anthropogenic sulfur and organic sources.

Size distributions measured in the southern hemisphere stratosphere (Fig. 11l) are unique from the tropospheric size

620   distributions, with almost no coarse mode and a composition dominated by nearly pure sulfuric acid, meteoric materials

mixed with sulfuric acid, and mixed sulfate/organic particles from the upper troposphere. During ATom, particles from three

specific events–a volcanic eruption, a pyro-cumulus injection, and lofting of dust–strongly influenced the stratospheric

aerosol during ATom; these cases are discussed in Murphy et al. (2020).

3.3.3 Modal parameters

625   Many global models use modal representations of the particle size distribution because sectional models are

computationally expensive. As described briefly in Sect. 2.4, and in more detail in the Supplemental Materials, the measured

size distributions were fitted using four lognormal functions, representing the nucleation, Aitken, accumulation, and coarse

modes. After fitting, the integrated number, surface, and volume were compared with those from the raw size distributions.

The number, surface, and volume from the four modes of the fitted and measured distributions were similar and highly

630   correlated, with regression slopes between 0.94 and 1.10 and r^2 values >0.86 (Supplemental Material Tables S2–S4). The

four-mode lognormal fits efficiently describe the measured size distributions, and provide measurement-based lognormal

parameters for comparison with prescribed values used in many global models. Further, the modal fits provide a physically

rational way to average size distributions together, since the average geometric mean diameter (D_g) and standard deviation

(σ_g) for an air mass can be calculated directly. If one were to instead average all of the size distributions in an air mass

635   together and then fit lognormal parameters, σ_g would be too large because the average size distribution is broader than the

individual size distributions contributing to that average. AOD and direct radiative forcing are sensitive to the value of σ_g (Brock et al., 2016b).

As an example of the fitted lognormal parameters, vertical profiles for the tropics of the Pacific and Atlantic (Fig. 12) show several interesting features. In the Pacific tropics, no statistically significant nucleation mode (concentration <30

640   cm^{-3}) was present at altitudes <5 km. Nucleation and Aitken mode concentrations decreased from values >10^4 cm^{-3} and >10^3 cm^{-3}, respectively, at the top of the profile to values ~10 cm^{-3} and ~200 cm^{-3} at 2 km as a result of new particle formation in the UT and coagulational loss during slow descent (Fig. 12a; Clarke et al., 2002; Williamson et al., 2019). Growth due to condensation during this descent is evident in the slightly increasing modal diameter of the Aitken and accumulation modes with decreasing altitude (Fig. 12b), although this growth is somewhat obscured by the shift in growing particles from the

645   nucleation mode to the Aitken mode. The σ_g values of the accumulation and Aitken modes tend to decrease with decreasing altitude in the troposphere (Figs. 12c,f), which is also consistent with condensational growth, which leads to a narrowing of the size distribution (McMurry and Wilson, 1982). The new particle formation in the tropical UT is tightly coupled to the very low concentrations of accumulation-mode particles (Fig. 12a) due to scavenging during deep convection (Clarke et al., 2002; Williamson et al., 2019). Nucleation-mode concentrations are lower in the UT over the Atlantic (Fig. 12d) than over

650   the Pacific (Fig. 12a), although the same general trend of declining concentration towards the surface remains.

The number concentration of coarse-mode particles declines rapidly with increasing altitude above the MBL, while accumulation-mode concentrations do not fall consistently with increasing altitude (Fig. 12a,d). Coarse-mode particle concentrations in the lower troposphere are consistently higher over the Atlantic than over the Pacific due to Saharan dust. The σ_g of the lognormal distribution for sea salt is >2 in the lowest 2 km of the profile, but <2 in the middle and upper

655   troposphere, where dust dominates the coarse mode. In general, the value of σ_g ranges from ~1.5 to ~2 for all modes througout the profiles except for the coarse sea-salt mode at altitudes <2 km.

Similar plots for the other regions measured during ATom are presented in the Supplemental Materials (Figs. S1–S2). The modal parameters from the ATom data are compared with two previously published datasets in Sect. 4.1.

3.3.4 Single scatter albedo and absorption

660   Single scatter albedo ω_0 is the ratio of light scattering to the sum of scattering and absorption. This parameter is key

in determining the direct radiative effect of aerosol (McComiskey et al., 2008). In most of the air masses encountered in

ATom, values of ω_0 at both dry and ambient RH conditions tend to decrease from values >0.96 near the surface to a broad

minimum in the lower or middle FT, before increasing again in the UT (Fig. 13). These profiles result because extinction

falls more rapidly with increasing altitude from the boundary layer to the FT than does absorption due to BC and BrC (Figs.

665   9, 13). This decrease in ω_0 in most of the profiles (Fig. 13) may be associated with the general shift of accumulation-mode

particles to smaller particle sizes with increasing altitude (Fig. 12), which would reduce their aerosol mass scattering

efficiency, while the mass absorption efficiency of absorbing BC particles does not change much with increasing altitude.

3.3.5 Cloud condensation nuclei

The concentrations of CCN at STP conditions, determined from the size distributions and calculated hygroscopicity

670   at five values of supersaturation, show substantial variations across the different regions sampled during ATom (Fig. 14). In

the midlatitudes of the Northern Hemisphere (Figs. 14c, d), concentrations are substantially higher at all altitudes than at

similar latitudes in the Southern Hemisphere (Figs. 14g, h). For example, at supersaturations of 0.2%, concentrations in the

Southern Hemisphere are ~10–50 cm^{-3} throughout the profile, while in the Northern Hemisphere the concentrations fall with

increasing altitude from >100 cm^{-3} in the MBL to ~50 cm^{-3} in the middle troposphere. In the tropics, concentrations fall

675   steadily from >200 cm^{-3} near the surface to ~10 cm^{-3} at 10 km altitude. The spread in CCN concentrations for the different

supersaturations increases with altitude in the tropics and northern midlatitudes due to the shift in concentration to smaller

sizes (Fig. 12). In the Arctic, Antarctic/Southern Ocean, and southern midlatitude profiles the CCN concentrations do not

spread with increasing altitude as much because the aerosol size distributions in these regions do not shift to smaller sizes

with increasing altitude (Supplemental Materials Figs. S1, S2).

680 **4. Discussion**

4.1 Comparison with previously published work

It is far beyond the scope of this work to provide a comprehensive comparison of the ATom observations with the

extensive literature on global aerosol microphysical properties, which are derived from a panoply of in situ and remote

sensing measurements and model simulations. However, it is useful to briefly compare the airborne data with two frequently

685 used datasets, the OPAC (Optical Properties of Aerosols and Clouds; Hess et al., 1998; Koepke et al., 2005) database, which

is commonly used by global models, and the more recent ship-borne dataset reported by Quinn et al. (2017). The

measurements of Quinn et al. (2017; hereafter Q17) were made from 1993–2015 during multiple research cruises over the

Arctic, Pacific, Southern, and Atlantic Oceans using a suite of instruments to obtain the particle size distribution from 0.02–

10 µm diameter at dry conditions. These observations are thus directly comparable to the dry Aitken, accumulation, and

690 coarse-mode size distributions measured in the MBL during ATom. In addition, we can compare our observations with the

modal aerosol model (MAM; Liu et al., 2012, 2020), which places various aerosol types into prescribed lognormal modes,

usually using 4 or 7 such modes.

Global models that use a modal description of aerosol size distributions often use the OPAC database to prescribe

lognormal parameters. The OPAC database provides lognormal parameters for several particle types, including "insoluble",

695 "water-soluble", "soot", and mineral particles in three different size classes: Aitken (referred to as "nucleation" in OPAC),

accumulation, and coarse modes, and sea salt in the latter two modes only. The OPAC database is meant to represent

"average" atmospheric conditions, presumably including polluted air masses, while the ATom dataset focuses on remote

marine air with aged aerosol from a mix of continental and marine sources.

The most direct comparisons between the ATom dataset and the OPAC database is between the "water-soluble",

700 "sea-salt", and "mineral" OPAC components and the sulfate/organic, sea salt, and dust aerosols measured during ATom. The

sulfate/organic particles are best described by modal fits to the Aitken and accumulation modes, while sea-salt and dust

particles are best described by the coarse mode fits. The comparisons (Fig. 15; Table S6) show that, in general, σ_g is wider in

the OPAC database than in the ATom observations, except for coarse-mode sea salt (in which case OPAC is lower than the

observations) and accumulation mode dust (in which case they are comparable). In contrast to OPAC, several versions of the

705   modal aerosol model (MAM), used in various earth system models (e.g., Liu et al., 2012, 2020), incorporate σ_g values that

range from 1.6 to 2.0 for the Aitken, accumulation, and coarse modes, which are much more aligned with the ATom and

Q17 measurements, except for coarse mode sea salt. The larger σ_g in the OPAC database for all aerosol types except sea salt

would tend to increase the amount of extinction and scattering per unit aerosol mass (Brock et al., 2016b), potentially leading

to an overprediction in AOD and direct radiative effect when the OPAC parameters are applied to the remote FT in global

710   models. Additionally, the geometric mean diameters, both for number and for volume, differ considerably between the

OPAC database and the ATom observations (Fig. 15a). For example, the accumulation-mode number geometric mean

diameter $D_{g,n}$ in the observations is approximately twice that of the OPAC "water-soluble" fraction. This may be in part

caused by the OPAC database including Aitken-mode particles in the "water-soluble" category.

       The comparisons between the ship-borne measurements in Q17 and the ATom measurements are more direct, as

715   both use similar modal fitting procedures and definitions for the modes, and are made primarily over the remote Pacific and

Atlantic oceans. The modal fits from ATom and from Q17 are generally quite consistent. The Aitken and accumulation

mode parameters are similar between ATom and the ship-borne measurements, with the range of ATom parameters

generally narrower than the Q17 parameters, which span a longer time period and larger range of meteorological conditions

than the airborne measurements. Both the Q17 and Atom data suggest values of σ_g <1.9 in the MBL for both the

720   accumulation and coarse modes, while the OPAC database has a significantly larger value of σ_g for these modes and all

aerosol types. For the coarse mode in the MBL, referred to as the "sea-spray" mode in Q17 and the "sea-salt" coarse mode in

the OPAC database, both the Q17 and ATom datasets report a value $D_{g,n}$ that is considerably smaller than that in OPAC and

MAM7, and a significantly larger σ_g. These differences are important, as sea salt is the single largest contributor to AOD

over the oceans (e.g., Haywood et al., 1999), and AOD (hence the direct radiative effect) is sensitive to these parameters

725   (Brock et al., 2016b).

4.2 Limitations of the ATom dataset

Although the combined ATom aerosol dataset offers a comprehensive and detailed picture of global-scale aerosol properties, it is limited in important ways. Most significantly, the ATom measurements do not represent a climatology, although they are representative of seasonally typical values for a subset of measured parameters that have been compared to

730   climatologies (Strode et al., 2018; Bourgeois et al. 2020). The four circuits around the globe, once in each season, provide a snapshot of aerosol conditions at those particular times without targeting specific phenomena, unlike most airborne projects. Comparisons between models and the ATom data will be most effective if meteorology and emissions are prescribed or nudged to match the times of the ATom flights, and if the model domain is sampled along the aircraft flight track. Similarly, comparisons with remote sensing measurements should overlap in space and time to the extent possible.

735   There are limitations to specific aspects of the data presented here, as well. The compositional data we consider in this combined dataset represent only a fraction of the richness of the data from the HR-TOF-AMS and PALMS spectrometers and of the filter-based bulk measurements. Data from these instruments include detailed information on molecular markers of specific sources and processes (e.g., *f57*, *f44*), ratios of H/C and O/C within OA (Hodzic et al., 2020), ionic balance and acidity (Nault et al., 2021), speciation of inorganic ions, and the presence of rare particle types (e.g.,

740   Murphy et al., 2018). Potential users of the data are encouraged to communicate with the instrument teams to make full use of the available information in their analyses.

The particle size distributions are measured using a condensation technique (the NMASS battery of CPCs) which report a Kelvin (condensation) diameter. These data are combined with an optical particle spectrometer (the UHSAS) which measures an optical size. Thus discontinuities can occur at the boundary between the instruments, at about 60 nm (Brock et

745   al., 2019). Unfortunately, this is near the critical diameter for CCN activation at typical water supersaturations for stratocumulus and cumulus clouds. Smoothing is used to minimize potential discontinuities. At diameters from 0.6–2 μm, the laser optical particle spectrometers are in a regime of Mie oscillations, where particle sizing is relatively insensitive, or even ambiguous. This can cause spurious high-frequency features in the size distribution in this size range, as noted in Sect.

3.3.2. These features, which are not smoothed, do not substantially affect the optical properties or modal parameters, but

750   could be misinterpreted as physical attributes.

The modal parameters fitted to the size distributions rely upon a priori assumptions regarding the number of modes and their characteristics (see Supplemental Materials). There are cases in the remote FT when the Aitken and accumulation modes are subjectively indistinguishable, yet the fitting procedure attempts to fit two modes. The user of the combined dataset is cautioned that there are times when the accumulation mode might actually be an extension of a single Aitken

755   mode. In addition, when there are very few coarse mode particles, the fitting algorithm may still attempt to describe the few counts present with lognormal parameters, leading to excessive variation in the modal parameters.

The composition of the coarse mode is measured using the PALMS instrument sampling behind an inlet that removes particles with $D_p > 4.8$ µm in the lower troposphere and > 3.2 µm in the UT (McNaughton et al., 2007). The composition of larger particles as measured by the underwing CAS instrument is assumed to be the same as those in the

760   largest PALMS size class (1.13 to ~4 µm). If the composition of particles with $D_p > 4$ µm measured by the CAS is different, this will produce a bias. This potential bias is likely to be small in the MBL since these larger particles are almost certainly sea-spray aerosol. In calculating optical properties, these coarse-mode particles are assumed to be spherical; no attempt has been made to simulate dust or sea salt properties using non-spherical approaches.

Finally, we have not attempted to propagate uncertainties beyond the size distribution uncertainties described by

765   Brock et al. (2019), based on comprehensive instrument evaluations by Kupc (2018) and Williamson (2018). The final average uncertainty in integrated particle volume is estimated to be +13/-28% for the accumulation mode when counting statistics are not a limiting factor. Aerosol volume determined independently from the size distributions and from the AMS instrument are highly consistent (Guo et al., 2020), which lends confidence to the measurements. Determining uncertainties associated with applying composition data to the size distributions, with calculating hygroscopic growth, or with determining

770   the resulting optical properties and CCN concentrations would require Monte Carlo simulations over a large number of parameters for each of $> 2.4 \times 10^4$ measurements, which is impractical. Comparisons of calculated dry extinction and absorption with directly measured values during ATom-4 (Fig. 4) suggest errors in dry extinction and absorption of <20%,

while comparisons of the derived AOD with directly measured values from nearby AERONET sites (Fig. 6) suggest that

accumulated errors in ambient extinction are <30%.

775 **5. Conclusions**

The ATom project made four surveys, once in each season, of the composition of the remote, oceanic troposphere

and portions of the lower stratosphere at high latitudes. The aircraft repeatedly profiled between ~160 m and ~12 km,

mapping out the vertical and horizontal variation in aerosol and gas-phase properties. We have combined dry aerosol

composition and size distribution measurements made over the remote Pacific and Atlantic Oceans, as well as over portions

780 of the Arctic and Antarctic, to comprehensively describe the chemical, microphysical, and optical characteristics of the

aerosol. Inorganic electrolyte composition was determined using an algebraic composition model, and aerosol water was

then estimated using κ-Köhler theory. From the hydrated, composition-resolved size distributions, we have calculated a

number of intrinsic and extrinsic parameters that are related to the climate effects of the aerosol. These parameters include

various optical properties at 10 wavelengths, cloud condensation nuclei concentrations at 5 supersaturations, and lognormal

785 fits to 4 modes of the particle size distribution. Mid-visible dry extinction and absorption coefficients calculated from the

composition-resolved size distributions were in excellent agreement with directly measured dry extinction and absorption

coefficients made with independent instruments during the ATom-4 deployment. Mid-visible AOD was calculated by

vertically integrating ambient extinction values during profiles, and agreed well with values directly measured with

AERONET sunphotometers, despite substantial distances between the profiles and the AERONET sites.

790 Initial findings from the combined dataset show that the remote Northern Hemisphere troposphere has more aerosol

from continental sources than does the Southern Hemisphere. Dust and sulfate/organic mixtures contribute substantially to

AOD in the middle troposphere over the midlatitude northern Pacific Ocean and the lower and middle troposphere over the

tropical Atlantic Oceans. Unsurprisingly, sea-salt particles and associated water dominate AOD over most of the remote

oceans, especially in the Southern Hemisphere, while BB particles contribute over the subtropical and tropical Atlantic

795 Ocean and to a lesser extent over the North Pacific. Single scatter albedo was found to vary substantially with altitude due to

changes in both composition and size. The geometric standard deviation of lognormal fits to the Aitken and accumulation modes generally lay between 1.5 and 2.0, narrower than values in some modal representations used in global models. Within the MBL, the lognormal parameters for these modes and for the coarse mode are generally consistent with values from extensive shipboard measurements in the remote oceans.

800   To our knowledge, this is the first time that such a broad range of directly measured aerosol size distributions, composition, and optical properties have been combined in a single, self-consistent dataset for use by the scientific community. These snapshots of atmospheric composition, while not representing a climatology with statistical information on time-varying properties, provide information that can help constrain model representations of aerosol emissions, transport, removal, and processing, as well as a priori assumptions used in retrievals of aerosol properties from remote

805   sensing measurements. The data are accessible for public scientific use as described in the data availability statement below.

Author Contributions. All authors contributed to the observations described in this manuscript. CAB, KDF, MD, CJW, GS, DMM, NLW, PCJ, LZ, and JMK performed the key analyses. CAB wrote the manuscript with significant contributions from KDF, MD, CJW, GS, DMM, NLW, PCJ, JLJ, JMK., JD, and JP.

810   *Competing Interests.* The authors declare that they have no conflicts of interest.

Disclaimer. The contents do not necessarily represent the official views of NOAA or of the respective granting agencies. The use or mention of commercial products or services does not represent an endorsement by the authors or by any agency.

Acknowledgements. This work was supported by NASA under awards NNH15AB12I, NNX15AJ23G, NNX15AH33A, NNH13ZDA001N, NNX15AT90G, 80NSSC19K0124, and 80NSSC18K0630, and by the U.S. National Oceanic and

815   Atmospheric Administration (NOAA) Atmospheric Chemistry, Carbon Cycle, and Climate Program. AK is supported by the Austrian Science Fund FWF's Erwin Schrodinger Fellowship J-3613. BW and MD have received funding from the European Research Council (ERC) under the European Union's Horizon 2020 Research and Innovation Programme under grant agreement No. 640458 (A-LIFE) and from the University of Vienna.

Data Availability. The data products described in this manuscript are being submitted to the Oak Ridge National Laboratory
820   Distributed Active Archive Center (ORNL DAAC; https://daac.ornl.gov) for permanent archival storage and open public
access. During the Discussion phase of this manuscript, data may be requested directly from the corresponding author.

Table 1. Aerosol properties calculated from the combined aerosol dataset and archived in files.

Parameter	Parameter identifier[1]	Method	wavelengths	Comments
Dry scattering	*scat_dry_ambpt*	Mie theory from composition-resolved size distribution using refractive indices in Table 2	all[2]	Calculated at ambient pressure and temperature; Sect. 2.7.1
Dry absorption from BC	*BC_abs_ambPT*	Core-shell Mie theory using air mass-averaged MAC multiplied by 60s BC mass concentration	all[2]	Calculated at ambient pressure and temperature; Sect. 2.7.1
Dry absorption from BrC	*BrC_abs_ambPT*	Bivariate fit between BrC absorption from filter extracts and PALMS biomass burning particles and BC mass concentrations	all[2]	Calculated at ambient pressure and temperature; Sect. 2.7.1; estimated factor of 3 uncertainty
Dry extinction	*ext_dry_ambPT*	Sum of dry scattering and absorption from BC and BrC	all[2]	Calculated at ambient pressure and temperature
Ambient scattering	*scat_ambRHPT*	κ-Köhler theory to estimate water content; Mie theory to calculate scattering	all[2]	Calculated at ambient pressure and temperature
Ambient extinction	*ext_ambRHPT*	Ambient scattering + dry absorption from BC and BrC	all[2]	Calculated at ambient pressure and temperature
Dry single scatter albedo	*SSA_dry*	Dry scattering and extinction	all[2]	Ratio of scattering to extinction
Ambient single scatter albedo	*SSA_ambRH*	Ambient scattering and extinction	all[2]	Ratio of scattering to extinction
Dry extinction Angstrom exponent	*ext_Angstrom_dry*	Fit to dry extinction across all wavelengths[1]	all[2]	least squares regression to Eq. 10
Ambient extinction Angstrom exponent	*ext_Angstrom_ambRH*	Fit to ambient extinction at all wavelengths[1]	all[2]	least squares regression to Eq. 10
UV-Vis absorption Angstrom exponent	*abs_Angstrom_UV_Vis*	Fit to sum of dry absorption from BC and BrC	340, 380, 405, 440, 532 nm	least squares regression to Eq. 10
Vis-IR absorption Angstrom exponent	*abs_Angstrom_Vis_IR*	Fit to dry absorption from BC	532, 550, 670, 940, 1020 nm	least squares regression to Eq. 10
Dry mass extinction efficiency	*MEE_dry*	Dry extinction and dry aerosol mass from composition resolved size distributions and densities in Table 2	all[2]	ratio of dry extinction to dry aerosol mass
Ambient mass extinction efficiency	*MEE_ambRH*	Ambient extinction and dry aerosol mass	all[2]	ratio of ambient extinction to dry aerosol mass
Mass absorption cross-section	*MAC*	Core-shell Mie theory applied to coated BC particles	all[2]	Ratio of BC absorption to BC mass; calculated for air mass averages only; Table S5
Dry asymmetry parameter	*asymmetry_dry*	Mie theory at dry conditions, not including absorbers	all[2]	Eq. 8
Ambient asymmetry parameter	*asymmetry_ambRH*	Mie theory at ambient conditions, not including absorbers	all[2]	Eq. 8
Ambient lidar backscatter ratio	*backscat_ratio_ambRH*	κ-Köhler theory to estimate water content; Mie theory to calculate backscattering and scattering	all[2]	Ratio of backscatter to extinction at ambient RH
Ambient lidar backscatter cross-section	*backscat_ambRH*	κ-Köhler theory to estimate water content; Mie theory to calculate backscattering, dry aerosol mass	all[2]	Ratio of backscatter at ambient RH to dry particle mass
Effective radius	*eff_radius*	Integration of size distribution	—	Ratio of 3rd moment of the size distribution to the 2nd moment
Hygroscopicity parameter κ	*kappa_ams*	Volume-weighted sum of κ values from AMS in Table 2	—	Algebraic calculation of electrolytic composition; literature values
f(RH)85%	*f_rh_85*	Ratio of calculated extinction at 85% Rh to that at dry conditions	532 nm only	

κ_{ext}	*kappa_ext*	Fit to calculated extinction at 0, 70, 80, and 85% RH	532 nm only	Fit to Eq. 9
CCN concentration	*CCN_005, CCN_010, CCN_020, CCN_050, CCN_100*	Integration of particle size distribution for $D_p>D_{crit, dry}$	—	Eq. 2, Sect. 2.6; calculated for supersaturations of 0.05%, 0.1%, 0.2%, 0.5%, and 1.0%
Lognormal parameters D_g, σ_g, N	*lognorm_coefs_nucl, lognorm_coefs_Aitken, lognorm_coefs_accum, lognorm_coefs_coarse*	Fits to volume for coarse and accumulation mode and to number for Aitken and nucleation modes.	—	Supplemental materials, Tables S2-S4.
Mass concentration of sulfate, organics, dust, BC, BrC, aerosol water	*sulfate, organics, nitrate, ammonium, sea_salt, dust, BC, BrC_est, aerosol_H2O, mass_fine, mass_coarse*	Integration of volume size distribution for each component multiplied by density from Table 2, separated into coarse ($D_p{\geq}1$ μm) and fine ($D_p{<}1$ μm).		Ammonium and nitrate from AMS applied to sulfate/organic class across all sizes
Ambient fine mode extinction fraction η	*FMF*	Coarse and accumulation-mode compositions applied to lognormal fits to those modes, then Mie theory used to calculate extinctions for each	all[2]	Aerosol water calculated using κ-Köhler theory & values from Table 2

[1]Identifier of variable (short name) in netCDF file
825   [2]340, 380, 405, 440, 532, 550, 670, 870, 940, 1020 nm

Table 2. Assumed values of hygroscopicity parameter κ, density ρ, and refractive index.

Instrument: Parameter	Hygroscopicity parameter κ^A	Reference	Density ρ (kg m^{-3})	Reference	Refractive Index	Reference
PALMS: sulfate/organic particles	$(1-F_{org})^B \times 0.483 + F_{org} \times 0.17^C$	Froyd et al. (2019)	$(1-F_{org}) \times 1770 + F_{org} \times 1350^C$	Froyd et al. (2019)	$((1-F_{org}) \times 1.479 + F_{org} \times 1.48) + 0i$	Froyd et al. (2019)
PALMS: biomass burning, oil combustion, meteoritic, and unclassified	$(1-F_{org}) \times 0.483 + F_{org} \times 0.17$	Froyd et al. (2019)	$(1-F_{org}) \times 1770 + F_{org} \times 1350^C$	Froyd et al. (2019)	$((1-F_{org}) \times 1.479 + F_{org} \times 1.48) + 0i$	Froyd et al. (2019)
PALMS: Soot (assumes small soot core with thick coating)	$(1-F_{org}) \times 0.483 + F_{org} \times 0.17$	Froyd et al. (2019)	$(1-F_{org}) \times 1770 + F_{org} \times 1350^C$	Froyd et al. (2019)	$((1-F_{org}) \times 1.479 + F_{org} \times 1.48) + 0i$	Froyd et al. (2019)
PALMS: Sea salt	1.1	Zieger et al. (2017)	1800^C	Froyd et al. (2019)	1.447+0i^D	Froyd et al. (2019)
PALMS: Mineral dust	0.03	Froyd et al. (2019)	2500	Froyd et al. (2019)	1.58+0.005i	Froyd et al. (2019)
PALMS: Alkali salts	0.5	Froyd et al. (2019)	1500	Froyd et al. (2019)	1.52+0i	Froyd et al. (2019)
SP2: Black Carbon	N/A^E		1800	Park et al. (2004)	2.26+1.26i	Moteki et al. (2010)
SP2: Coating	N/A^E		N/A^E		1.44+0i	mean of AMS for all of ATom
Calculated: H$_2$O	N/A^E		1000		1.33+0i	Hale and Querry (1973)
AMS: (NH$_4$)$_2$SO$_4$	0.483	Good et al. (2010)	1760	Hand and Kreidenweis (2002)	1.527+0i	Hand and Kreidenweis (2002)
AMS: (NH$_4$)HSO$_4$	0.543	Good et al. (2010)	1780	Hand and Kreidenweis (2002)	1.479+0i	Hand and Kreidenweis (2002)
AMS: (NH$_4$)$_3$H(SO$_4$)$_2$	0.579	Good et al. (2010)	1830	Hand and Kreidenweis (2002)	1.53+0i	Hand and Kreidenweis (2002)
AMS: H$_2$SO$_4$	0.87	Petters and Kreidenweis (2007)	1800	Hand and Kreidenweis (2002)	1.408+0i	Hand and Kreidenweis (2002)
AMS: NH$_4$NO$_3$	0.597	Good et al. (2010)	1725	Tang, 1996	1.553+0i	Tang (1996)
AMS: NH$_4$Cl	0.5	assumed^F	1519	Haynes et al. (2014)	1.64+0i	Haynes et al. (2014)
AMS: HNO$_3$	0.999	Good et al. (2010)	1513	Haynes et al. (2014)	1.393+0i	Haynes et al. (2014)
AMS: HCl	0.5	assumed	1490	Haynes et al. (2014)	1.329+0i	Haynes et al. (2014)
AMS: OA	$0.19 \times (O/C) - 0.0048^G$ Mean=0.179	Rickards et al. (2013)	1550^C	Guo et al. (2020) average from ATom-1 and -2	1.48+0i	Varma et al. (2013)

830   ^{A}PALMS κ values are applied to refractory and non-refractory components for all $D_p>0.25$ µm. AMS values are applied to all non-refractory components for $D_p \leq 0.25$µm. The Zaveri et al. (200x) composition model provides speciation of AMS components.
$^B F_{org}$ is the ratio of organic to organic+sulfate mass in that size class determined by the PALMS instrument.
^{C}Organic density applied to PALMS is chosen from Froyd et al. (2019) for consistency with other PALMS data products, but is inconsistent with AMS-derived density from Guo et al. (2020) applied here to AMS data.
835   ^{D}Assumes 27% residual water by mass (Froyd et al., 2019).
^{E}Not applicable: this parameter not used in any calculations.
^{F}Assumed value is not critical because these species are an insignificant part (<0.5%) of the total fine aerosol mass.
^{G}O/C is the O:C ratio from the HR-ToF-AMS measurements. The O:C ratios are smoothed with a running 10-point binomial filter (across ~10 minutes of data) before this equation is applied.

840
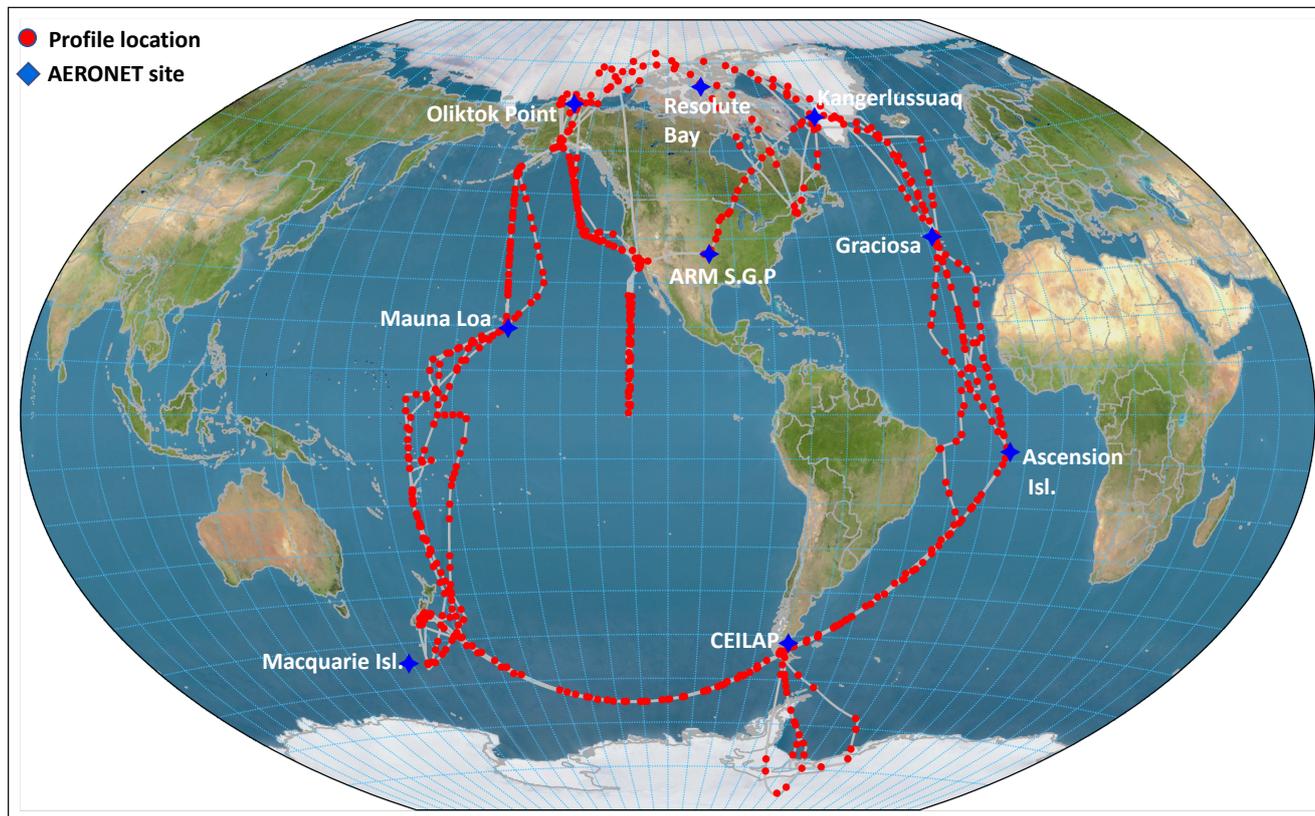
Figure 1. Map showing the flight track of the DC-8 aircraft (grey lines) and midpoint location of each vertical profile (ascent or descent; red circles). Locations and names of AERONET sites against which calculated AOD is compared are shown by blue diamonds and labels. Custom map produced using 1 km digital elevation model data from NOAA (https://www.ngdc.noaa.gov/mgg/topo/globe.html; last accessed 3 February 2016).

845
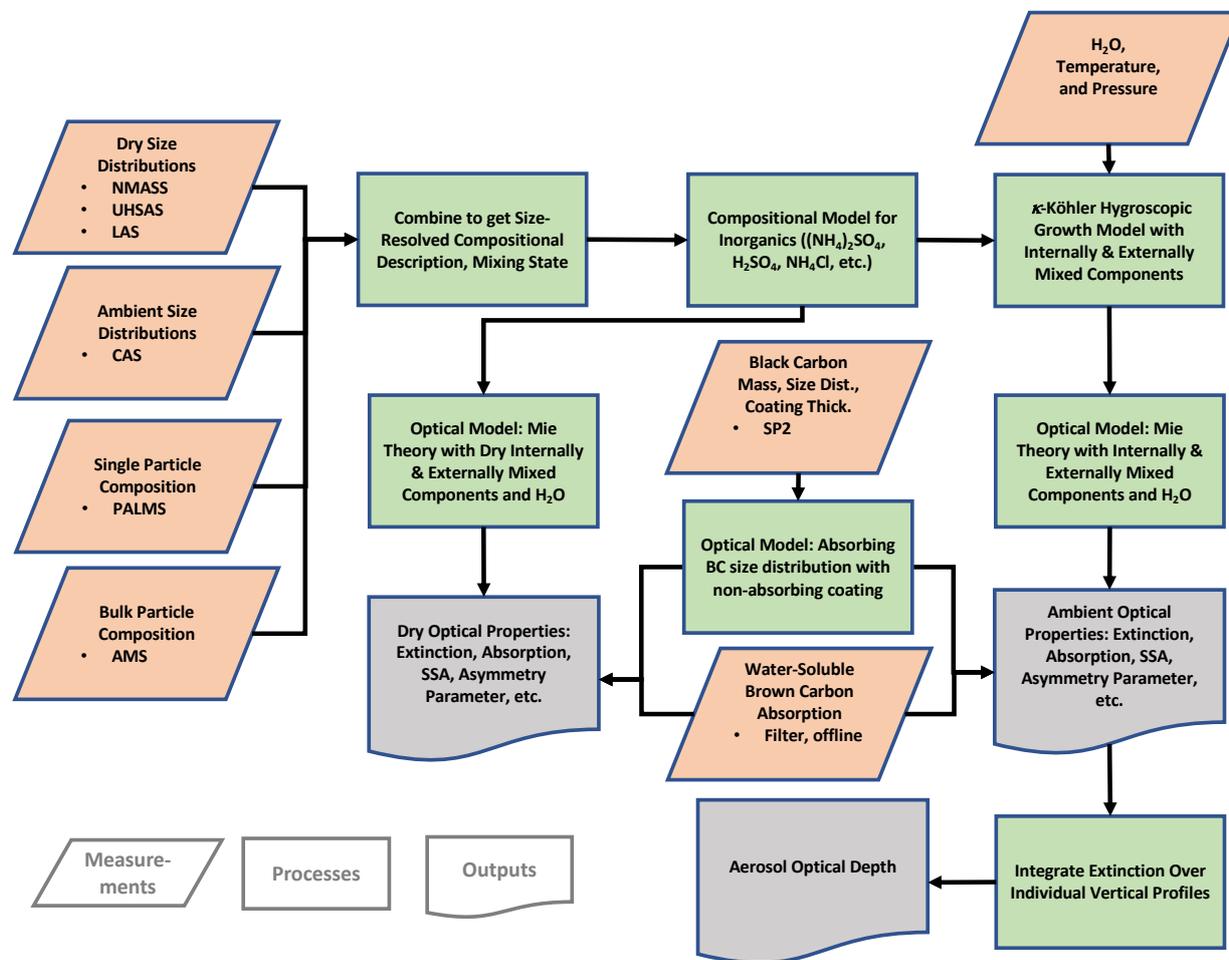
Figure 2. Schematic showing how data from instruments that measure size distribution, particle composition and meteorological parameters are combined to form a self-consistent description of the composition-dependent size distribution. Compositional, hygroscopic growth, and optical models are combined to determine dry and ambient aerosol optical properties and AOD.

850
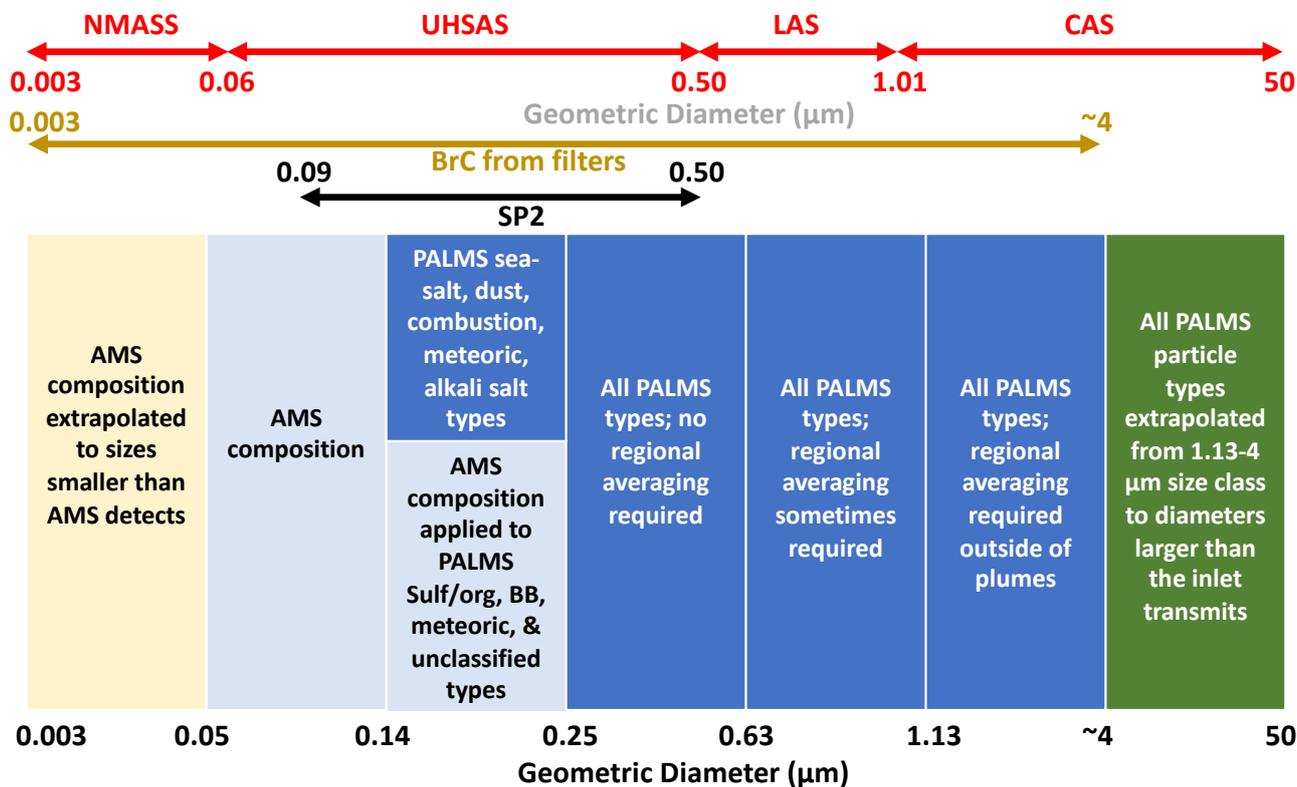
Figure 3. Schematic showing the portions of the size ranges of the particle size distribution instruments that are used, and the size ranges over which the composition measurements from the filter measurements, the SP2, the AMS, and the PALMS are applied. The need to average PALMS data to achieve statistically significant descriptions of particle composition are shown, as are the extrapolations of AMS and PALMS data to sizes where no compositional information are available.

855
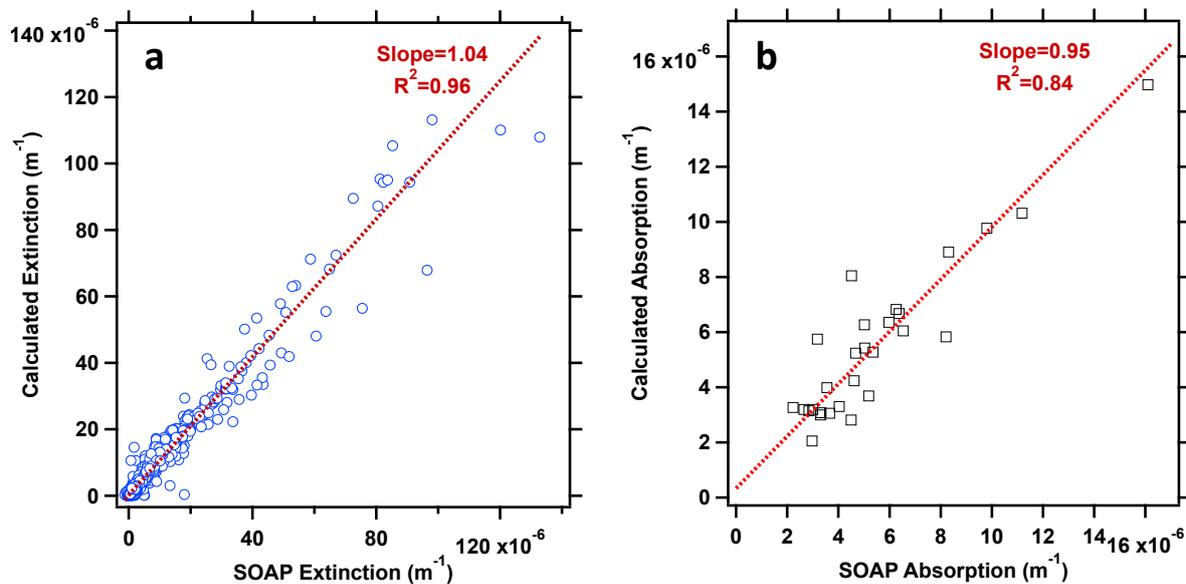
Figure 4. a) Calculated aerosol extinction as a function of measured extinction from the SOAP instrument during ATom-4. b) As in (a), but for calculated aerosol absorption and measured SOAP absorption for cases when absorption $>2\times10^{-6}$ m^{-1}. Lines and slopes are from two-sided (orthogonal distance) linear regressions; r^2 values are from one-sided fits. The bifurcation in the relationship between calculated and measured extinction at values $>40\times10^{-6}$ m^{-1} in (a) was not caused by any evident changes in aerosol composition or refractive index.
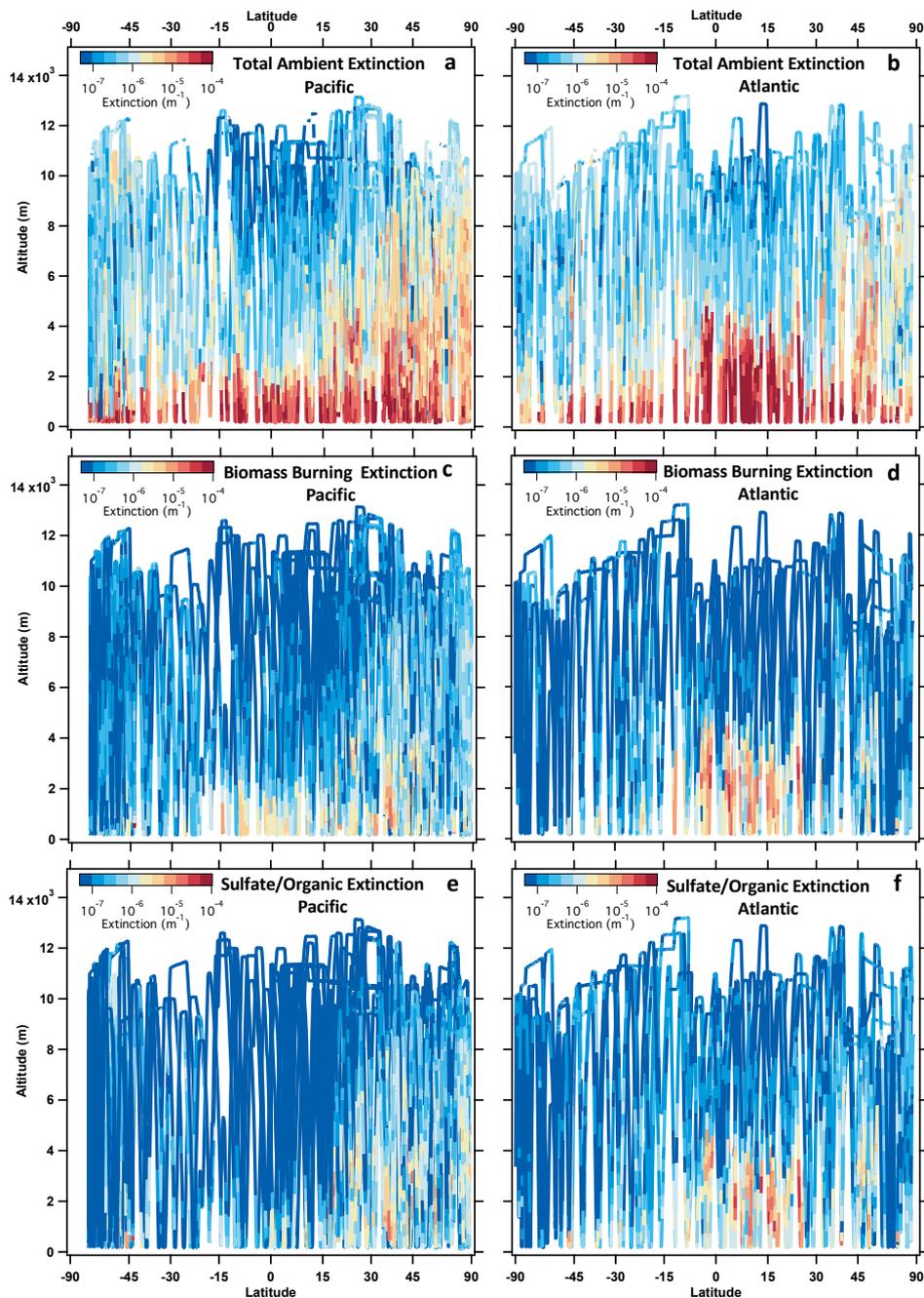
Figure 5. Altitude as a function of latitude color coded by extinction for all ATom deployments. X-axis is scaled to be proportional the Earth's surface area. Left column shows measurements made over the Pacific Ocean, western Arctic, and Southern Ocean; right column over the Atlantic, eastern Arctic, and Antarctic Peninsula (see Fig. 1). (a) and (b), total ambient extinction; (c) and (d), dry extinction from biomass burning particles; (e) and (f), dry extinction from mixed sulfate/organic particles.
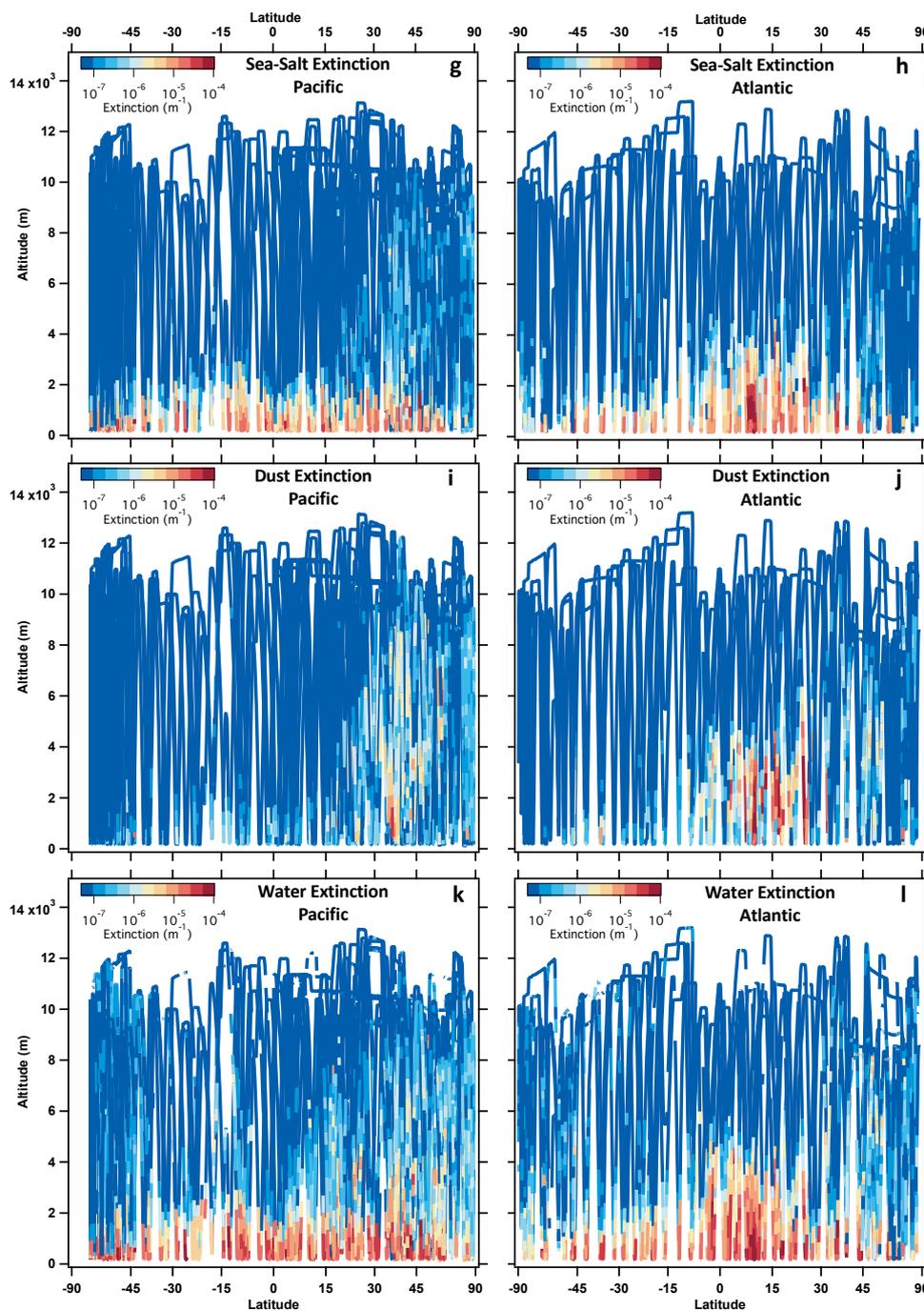
Figure 5 (continued). (g) and (h), dry extinction from sea-salt particles; (i) and (j), dry extinction from dust particles; (k) and (l), extinction from water associated with all particle types, based on κ-Köhler hygroscopic growth model.
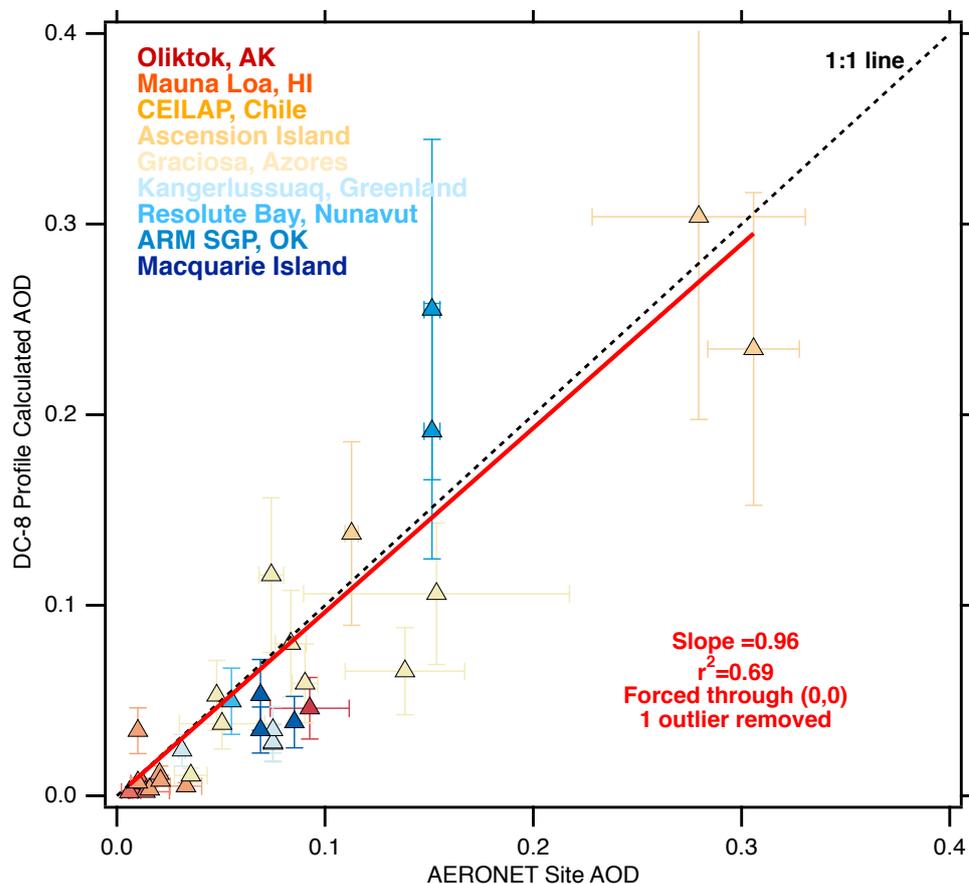
Figure 6. Aerosol optical depth (AOD) at 532 nm calculated from the in situ aerosol measurements on the DC-8 as a function of AOD measured by AERONET sites within 300 km and ±4 hours of the profile. AERONET AOD at 532 nm is interpolated from measurements at 500 and 670 nm following Eq. 10. One outlier data point has been removed. Two-sided linear regression (red line) was forced through the origin. Horizontal error bars indicate the variability in the AERONET AOD in ±4 hours surrounding the measurement time. Vertical error bars indicate an approximate ±30% uncertainty in the AOD derived from in situ measurements. Locations of the AERONET sites are given in Fig. 1.

880
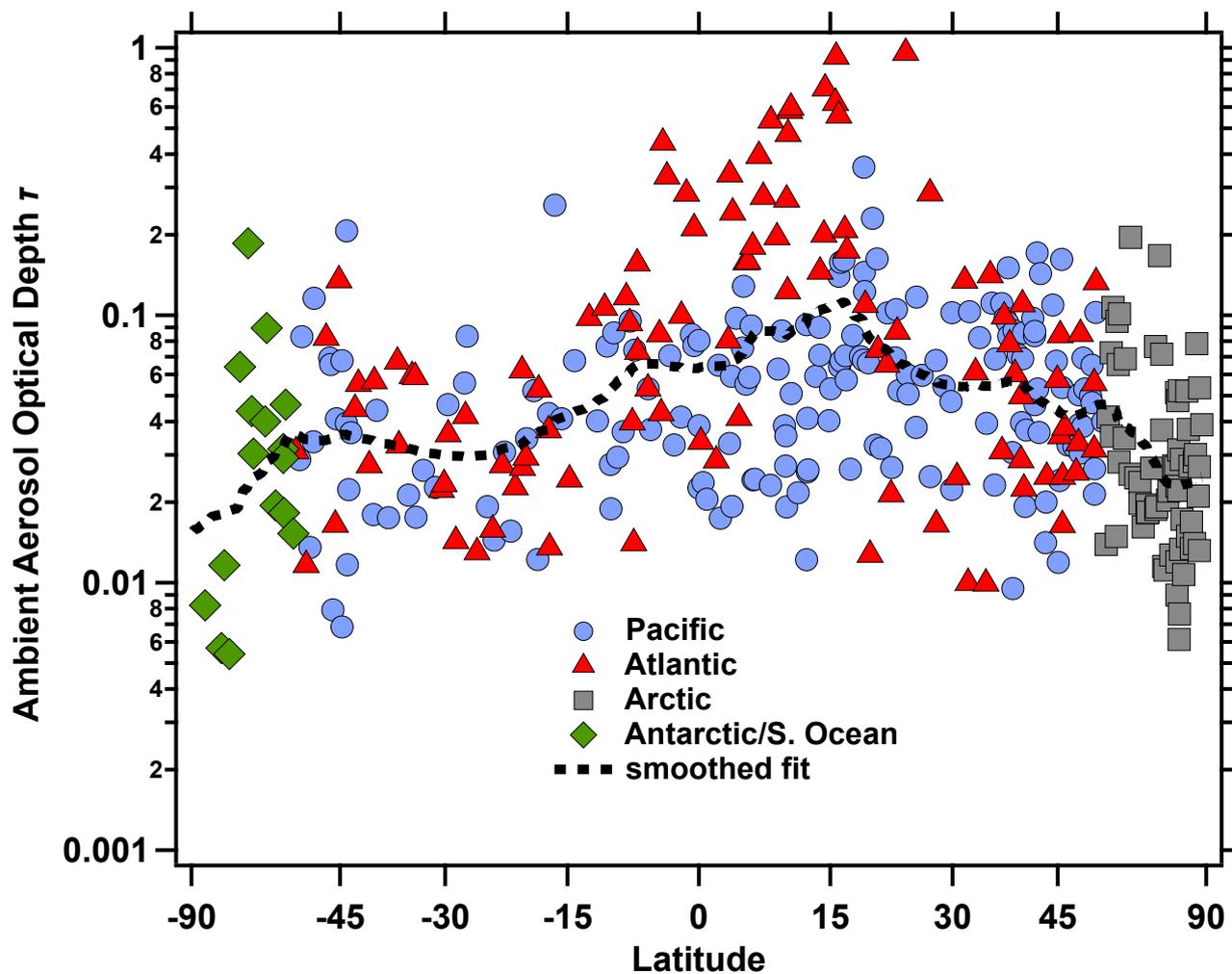
885

Figure 7. Ambient AOD calculated from in situ measurements as a function of latitude. Symbols indicate data taken over the Atlantic, Pacific, Southern Ocean and Antarctica, and the Arctic, with these regions described in Table S1. The smoothed dashed line is calculated using a locally weighted linear (LOWESS) regression.
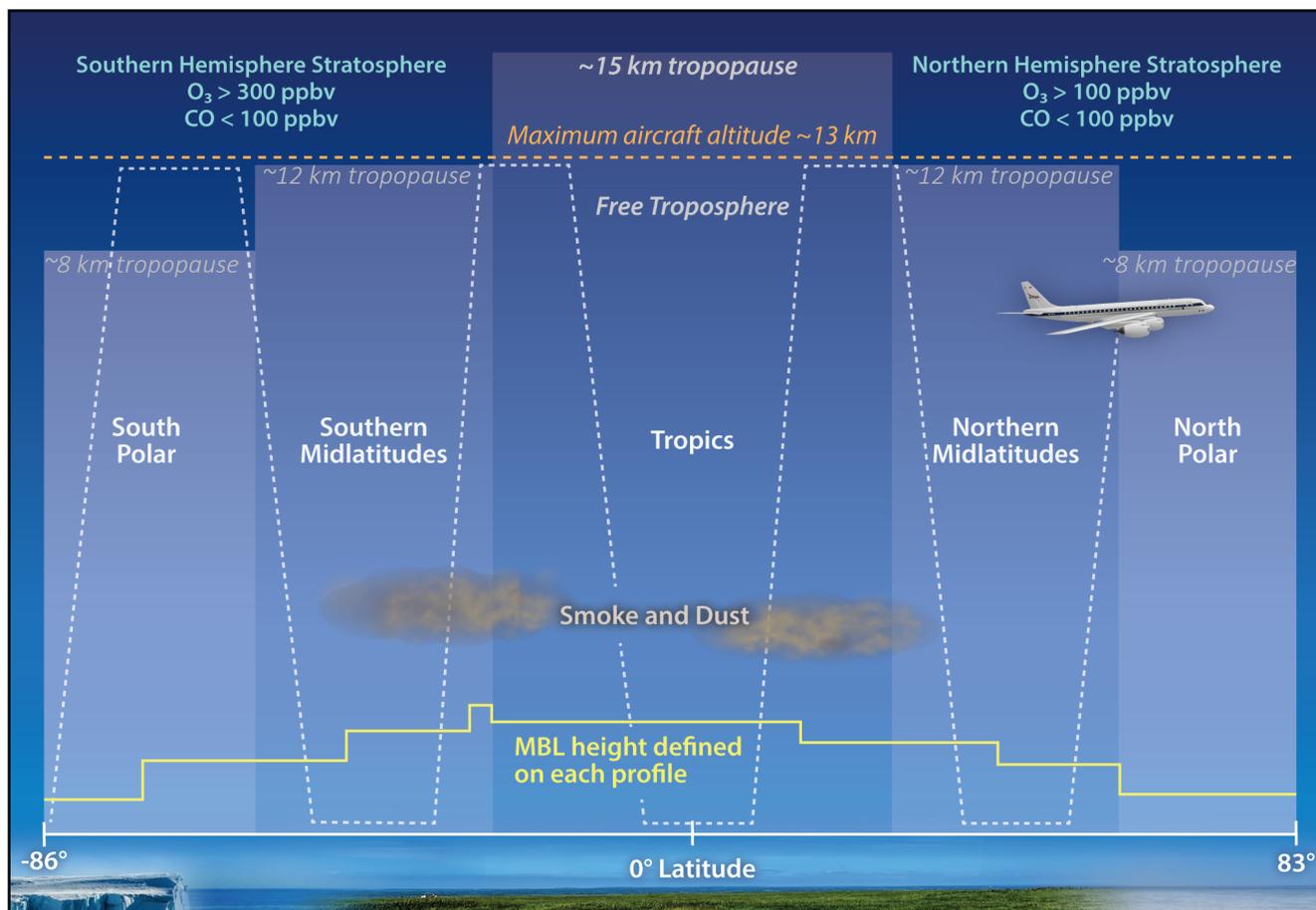
Figure 8. Schematic representation of the air mass classification scheme. The boundaries between the polar, midlatitude, and tropical air masses vary for each ATom deployment and ocean basin, and are listed in Table S1 in the Supplemental Materials. Data taken in biomass burning smoke ("smoke") and mineral dust ("dust") plumes are combined when concentration criteria are met (Sect. 2.3) regardless of latitude, while stratospheric regions are separated into northern or southern hemispheres because of different aerosol characteristics in each (Murphy et al., 2020).

890

895
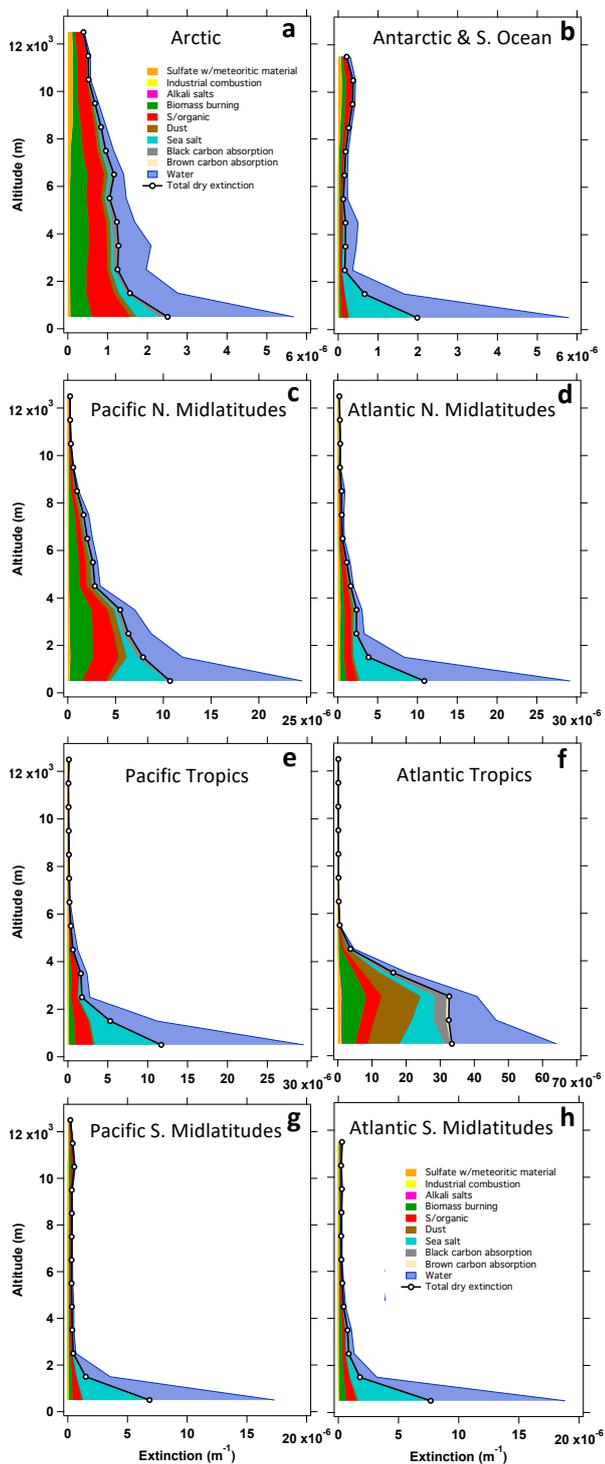
Figure 9. Average vertical profiles of extinction from each of the aerosol types, for different regions, across all of the ATom deployments. Note that scales on the x-axes vary.

900 **Descriptions of the regions are given in Fig. 8 and Table S1.**
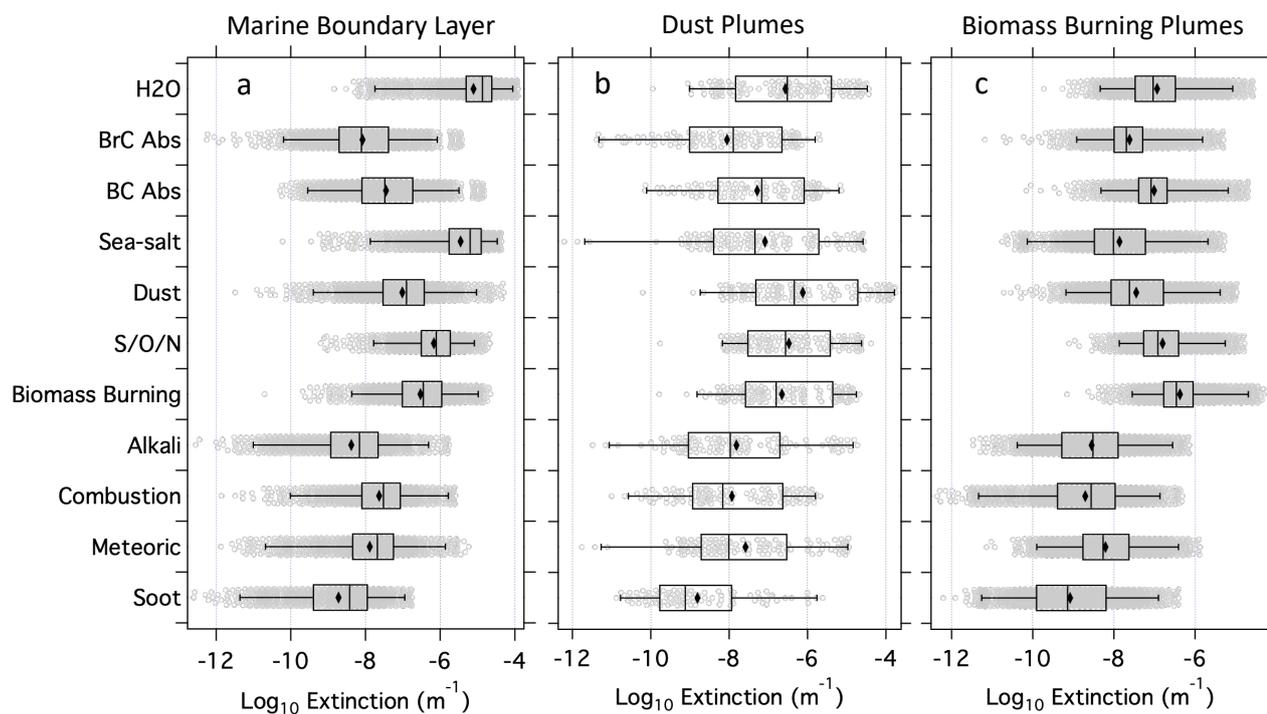
Figure 10. Contributions of different aerosol components to logarithm of aerosol extinction (a) in the MBL, (b) in dust plumes, and (c) in biomass burning plumes. Each gray point is calculated from a single 60 s measurement. Boxes indicate the interquartile range, the central line represents the median, the diamond symbol the mean of the logarithm, and the whiskers are at the 2nd and 98th percentiles. The row labeled "soot" is from the PALMS "EC" class, which represents only a small fraction of the BC particles present.
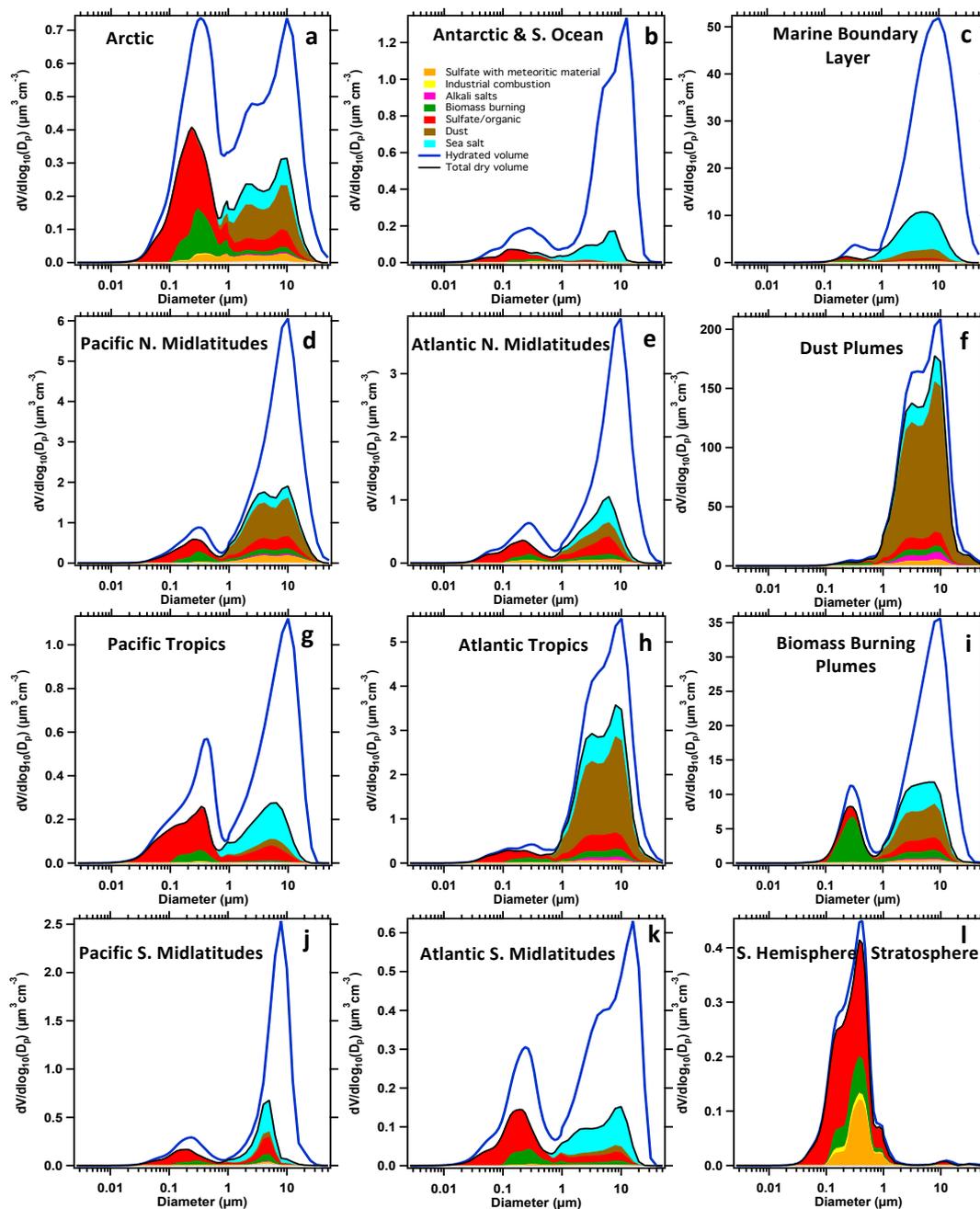
Figure 11. Volume of particles of different aerosol types as a function of diameter, averaged over all data in different regions and air mass types across all of the ATom deployments. Note that scales on the y-axes vary. Descriptions of the regions are given in Fig. 7 and Table S1. Regional data (left two columns) are from the FT only and exclude data from BB and dust plumes and stratospheric intrusions. Size distributions from the MBL, stratosphere, and BB and dust plumes (right column) are not separated by ocean basin or latitude range.
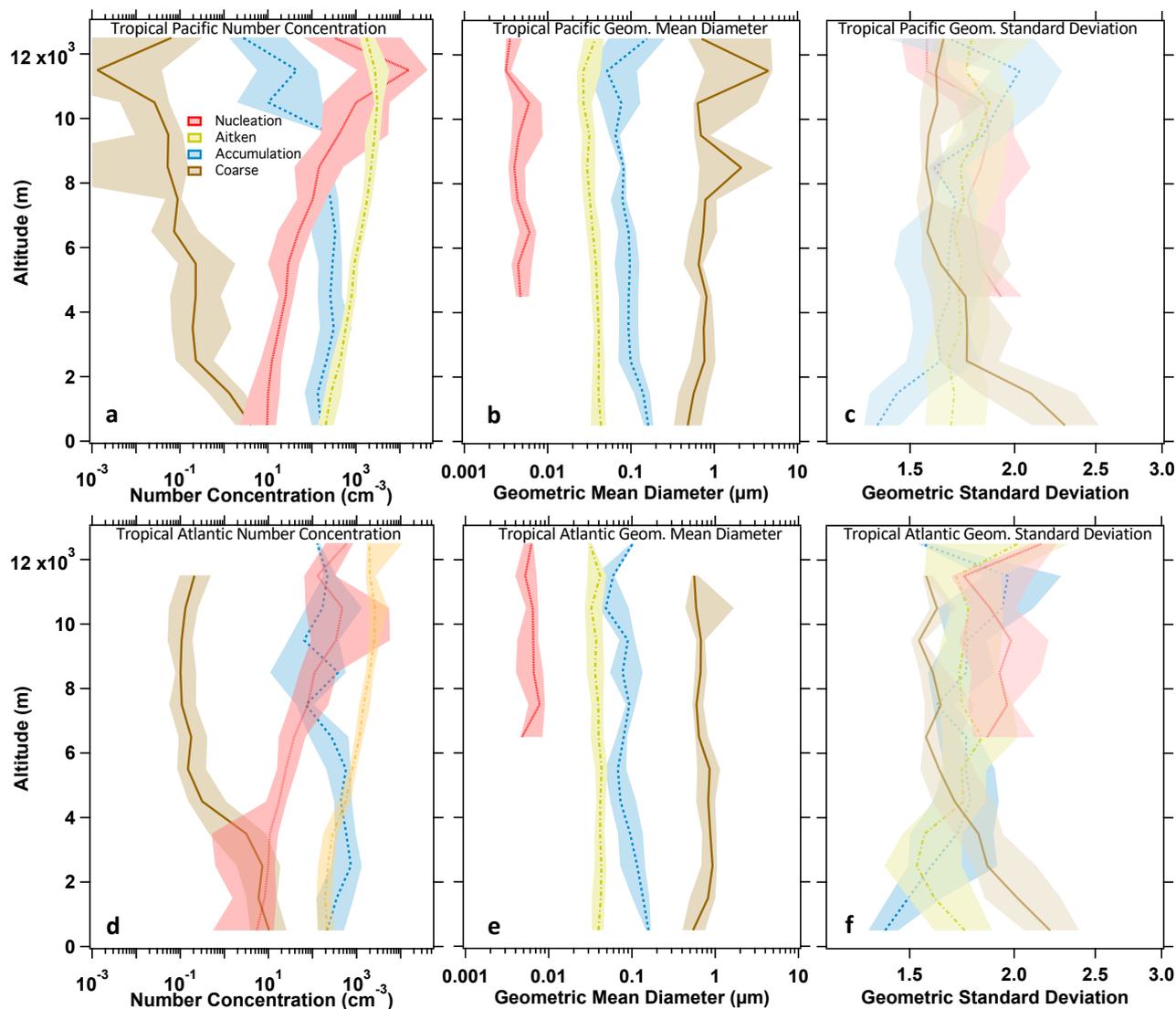
Figure 12. Vertical profiles of fitted lognormal parameters for the nucleation, Aitken, accumulation and coarse modes for the
Pacific tropics (a, b, and c) and the Atlantic tropics (d, e, and f) for the entire ATom project. Lines are median values and shaded
regions show the interquartile range. Number concentrations for the nucleation mode extend to lower altitudes than do the
geometric mean diameter and standard deviation because samples with very low or zero concentrations could not be fitted, yet still
provide valid concentration data that should be averaged. Similar vertical profiles for other regions sampled during ATom are in
Supplemental Materials Figs. S1-2.
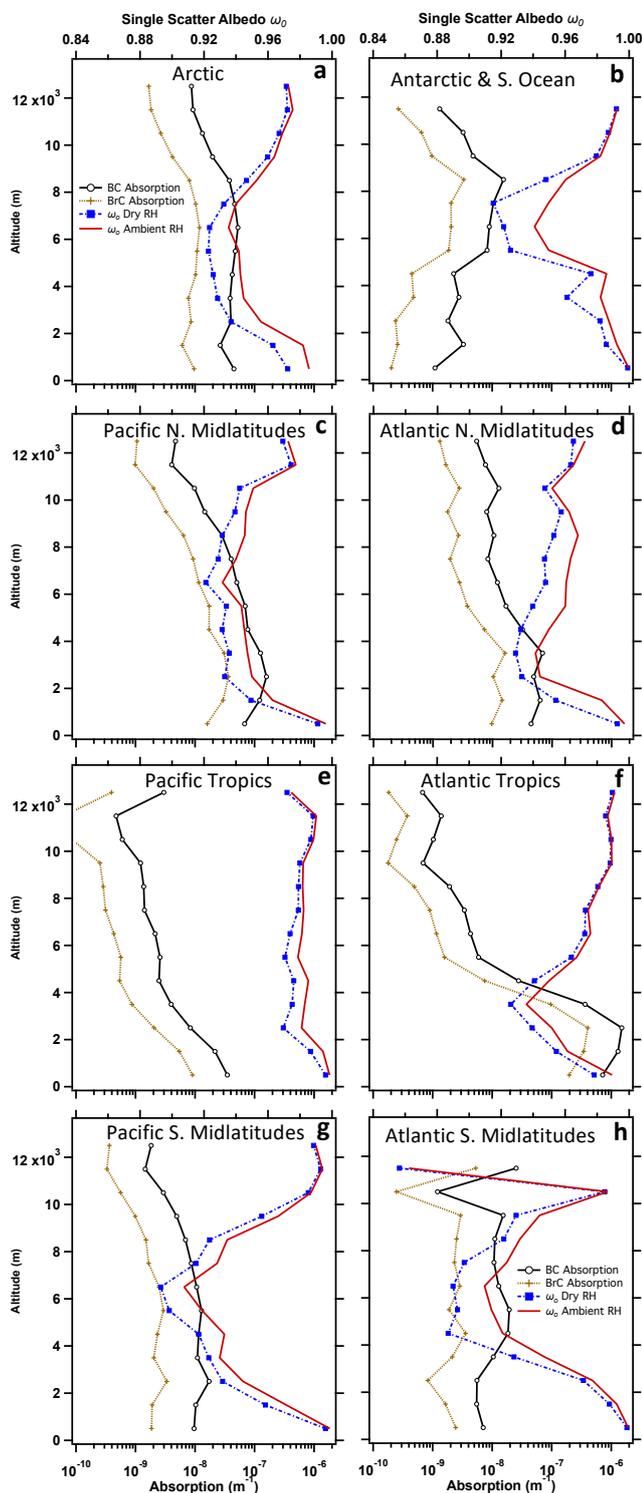
Figure 13. Median vertical profiles of absorption from BC and BrC (bottom axis) and single scatter albedo ω_0 at dry and ambient RH conditions (top axis) for different regions sampled during the entire ATom project. a) Arctic. b) Antarctic and Southern Ocean. c) Pacific northern midlatitudes. d) Atlantic northern midlatitudes. e) Pacific tropics. f) Atlantic tropics. g) Pacific southern midlatitudes. h) Atlantic southern midlatitudes.
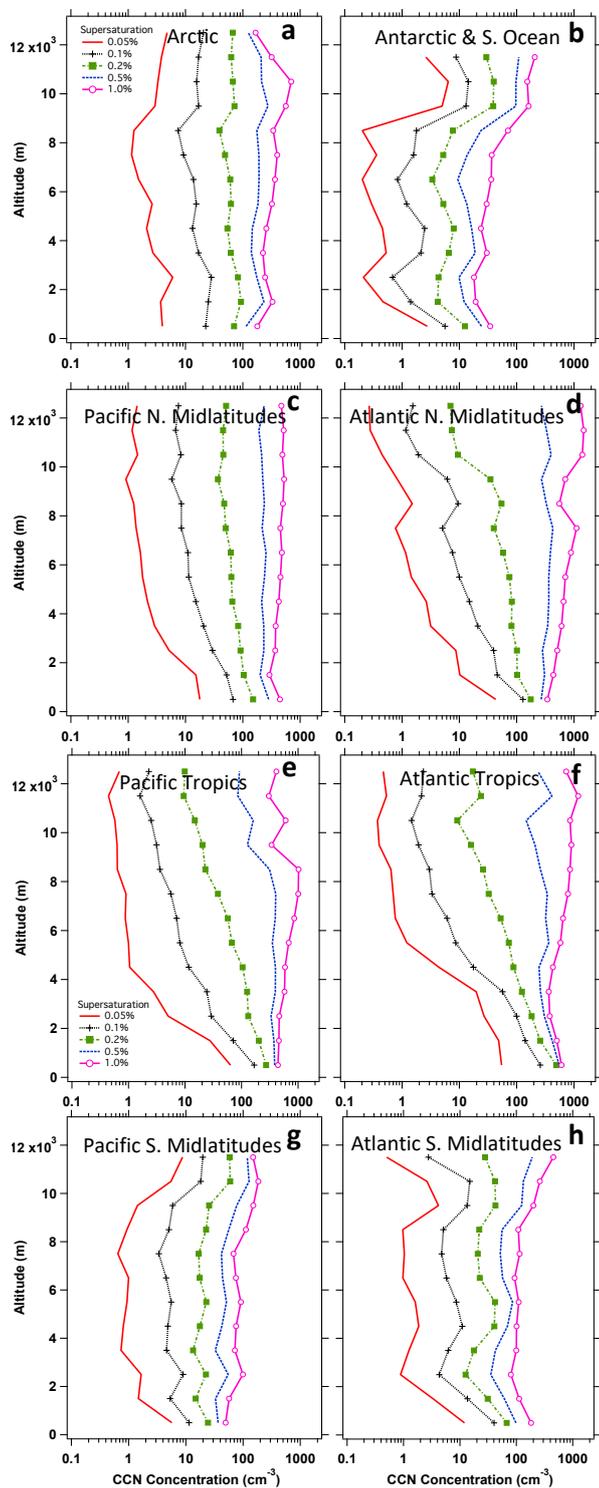
Figure 14. Median vertical profiles of calculated CCN concentration at STP for supersaturations of 0.05, 0.1, 0.2, 0.5, and 1% for different regions sampled during the entire ATom project. a) Arctic. b) Antarctic and Southern Ocean. c) Pacific northern midlatitudes. d) Atlantic northern midlatitudes. e) Pacific tropics. f) Atlantic tropics. g) Pacific southern midlatitudes. h) Atlantic southern midlatitudes.
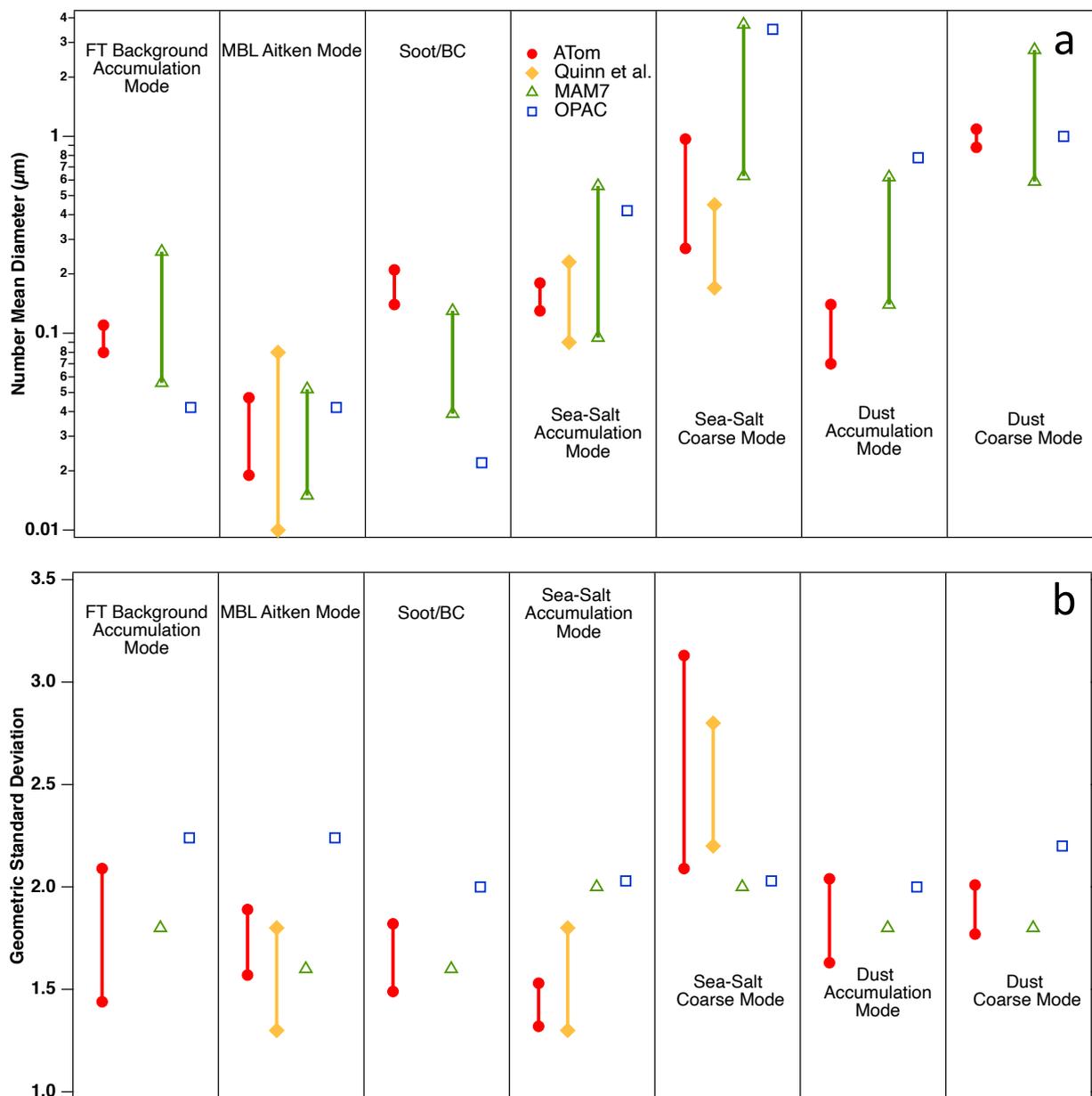
Figure 15. Lognormal parameters for different aerosol types from fits to the ATom dataset (showing interquartile range), from fits to shipboard size distribution measurements on the remote oceans (Quinn et al., 2017, showing full range), from the MAM7 modal aerosol model (Liu et al., 2012; 2020, showing interdecile range), and from the OPAC parameterization (Hess et al., 1998). a) Number geometric mean diameter; b) geometric standard deviation. The MAM7 parameterization provides a single fixed value of geometric standard deviation but a range of diameters for each aerosol type.

References

Anderson, T. L., Wu, Y., Chu, D. A., Schmid, B., Redemann, J., and Dubovik, O. : Testing the MODIS satellite retrieval of aerosol fine-mode fraction, J. Geophys. Res., 110, D18204, https://doi.org/10.1029/2005JD005978, 2005.

950   Andrews, E., Sheridan, P. J., Fiebig, M., McComiskey, A., Ogren, J. A., Arnott, P. Covert, D., Elleman, R., Gasparini, R., Collins, D., Jonsson, H., Schmid, B., Wang, J.: Comparison of methods for deriving aerosol asymmetry parameter, J. Geophys. Res., 111, D05S04, https://doi.org/10.1029/2004JD005734, 2006.

Andrews, E., Ogren, J. A., Kinne, S., and Samset, B.: Comparison of AOD, AAOD and column single scattering albedo from AERONET retrievals and in situ profiling measurements, Atmos. Chem. Phys., 17, 6041–6072,

955   https://doi.org/10.5194/acp-17-6041-2017, 2017.

Baumgardner, D., Jonsson, H., Dawson, W., O'Connor, D. and Newton, R.: The cloud, aerosol and precipitation spectrometer: a new instrument for cloud investigations, Atmos. Res., 59–60, 251-264, https://doi.org/10.1016/S0169-8095(01)00119-3, 2001.

Bohren, C. F. and Huffman, D. R.: *Absorption and Scattering of Light by Small Particles*, John Wiley & Sons, New

960   York, NY, ISBN: 978-0-471-29340-8, 1998.

Bond, T. C., Doherty, S. J., Fahey, D. W., Forster, P. M., Berntsen, T., DeAngelo, B. J., Flanner, M. G., Ghan, S., Kärcher, B., Koch, D., Kinne, S., Kondo, Y., Quinn, P. K., Sarofim, M. C., Schultz, M. G., Schulz, M., Venkataraman, C., Zhang, H., Zhang, S., Bellouin, N., Guttikunda, S., K., Hopke, P. K., Jacobson, M. Z., Kaiser, J. W., Klimont, Z., Lohmann, U., Schwarz, J. P., Shindell, D., Storelvmo, T., Warren, S. G., and Zender, C. S.: Bounding the role of black carbon in the

965   climate system: A scientific assessment, J. Geophys. Res. Atmos., 118, 5380– 5552, 2013.doi:10.1002/jgrd.50171, 2013.

Brock, C. A., Cozic, J., Bahreini, R., Froyd, K. D., Middlebrook, A. M., McComiskey, A., Brioude, J., Cooper, O. R., Stohl, A., Aikin, K. C., de Gouw, J. A., Fahey, D. W., Ferrare, R. A., Gao, R.-S., Gore, W., Holloway, J. S., Hübler, G., Jefferson, A., Lack, D. A., Lance, S., Moore, R. H., Murphy, D. M., Nenes, A., Novelli, P. C., Nowak, J. B., Ogren, J. A.,

Peischl, J., Pierce, R. B., Pilewskie, P., Quinn, P. K., Ryerson, T. B., Schmidt, K. S., Schwarz, J. P., Sodemann, H.,
970   Spackman, J. R., Stark, H., Thomson, D. S., Thornberry, T., Veres, P., Watts, L. A., Warneke, C., and Wollny, A. G.:
        Characteristics, sources, and transport of aerosols measured in spring 2008 during the Aerosol, Radiation, and Cloud
        Processes Affecting Arctic Climate (ARCPAC) Project, Atmos. Chem. Phys., 11, 2423–2453, https://doi.org/10.5194/acp-
        11-2423-2011, 2011.

        Brock, C. A., Wagner, N. L., Anderson, B. E., Attwood, A. R., Beyersdorf, A., Campuzano-Jost, P., Carlton, A. G.,
975   Day, D. A., Diskin, G. S., Gordon, T. D., Jimenez, J. L., Lack, D. A., Liao, J., Markovic, M. Z., Middlebrook, A. M., Ng, N.
        L., Perring, A. E., Richardson, M. S., Schwarz, J. P., Washenfelder, R. A., Welti, A., Xu, L., Ziemba, L. D., and Murphy, D.
        M.: Aerosol optical properties in the southeastern United States in summer – Part 1: Hygroscopic growth, Atmos. Chem.
        Phys., 16, 4987–5007, https://doi.org/10.5194/acp-16-4987-2016, 2016a.

        Brock, C. A., Wagner, N. L., Anderson, B. E., Beyersdorf, A., Campuzano-Jost, P., Day, D. A., Diskin, G. S.,
980   Gordon, T. D., Jimenez, J. L., Lack, D. A., Liao, J., Markovic, M. Z., Middlebrook, A. M., Perring, A. E., Richardson, M. S.,
        Schwarz, J. P., Welti, A., Ziemba, L. D., and Murphy, D. M.: Aerosol optical properties in the southeastern United States in
        summer – Part 2: Sensitivity of aerosol optical depth to relative humidity and aerosol parameters, Atmos. Chem. Phys., 16,
        5009–5019, https://doi.org/10.5194/acp-16-5009-2016, 2016b.

        Brock, C. A., Williamson, C., Kupc, A., Froyd, K. D., Erdesz, F., Wagner, N., Richardson, M., Schwarz, J. P., Gao,
985   R.-S., Katich, J. M., Campuzano-Jost, P., Nault, B. A., Schroder, J. C., Jimenez, J. L., Weinzierl, B., Dollner, M., Bui, T.,
        and Murphy, D. M.: Aerosol size distributions during the Atmospheric Tomography Mission (ATom): methods,
        uncertainties, and data products, Atmos. Meas. Tech., 12, 3081–3099, https://doi.org/10.5194/amt-12-3081-2019, 2019.

        Burgos, M. A., Andrews, E., Titos, G., Benedetti, A., Bian, H., Buchard, V., Curci, G., Kipling, Z., Kirkevåg, A.,
        Kokkola, H., Laakso, A., Letertre-Danczak, J., Lund, M. T., Matsui, H., Myhre, G., Randles, C., Schulz, M., van Noije, T.,
990   Zhang, K., Alados-Arboledas, L., Baltensperger, U., Jefferson, A., Sherman, J., Sun, J., Weingartner, E., and Zieger, P.: A
        global model–measurement evaluation of particle light scattering coefficients at elevated relative humidity, Atmos. Chem.
        Phys., 20, 10231–10258, https://doi.org/10.5194/acp-20-10231-2020, 2020.

Canagaratna, M., Jayne, J., Jimenez, J., Allan, J., Alfarra, M., Zhang, Q., Onasch, T. B., Drewnick, F., Coe, H., Middlebrook, A. M., Delia, A., Williams, L. R., Trimborn, A. M., Northway, M. J., DeCarlo, P. F., Kolb, C. E., Davidovits, P., and Worsnop, D. R.: Chemical and microphysical characterization of ambient aerosols with the Aerodyne aerosol mass spectrometer, Mass Spec. Rev., 26, 185–222, 2007.

Chin, M., Paul Ginoux, P., Kinne, S., Torres, O., Holben, B. N., Duncan, B. N., Martin, R. V., Logan, J. A., Higurashi, A., and Nakajima, T.: Tropospheric aerosol optical thickness from the GOCART model and comparisons with satellite and sun photometer measurements. J. Atmos. Sci., 59, 461–483, https://doi.org/10.1175/1520-0469(2002)059<0461:TAOTFT>2.0.CO;2, 2002.

Clarke, A. D., and Kapustin, V. N.: A Pacific aerosol survey. Part I: A decade of data on particle production, transport, evolution, and mixing in the troposphere, J. Atmos. Sci., 59, 363–382, https://doi.org/10.1175/1520-0469(2002)059<0363:apaspi>2.0.co;2, 2002.

DeCarlo, P. F., Kimmel, J. R., Trimborn, A., Northway, M. J., Jayne, J. T., Aiken, A. C., Gonin, M., Fuhrer, K., Horvath, T., Docherty, K. S., Worsnop, D. R., and Jimenez, J. L.: Field-deployable, high-resolution, time-of-flight aerosol mass spectrometer, Anal. Chem., 78, 8281–8289, doi:10.1021/ac061249n, 2006.

Dubovik, O., Smirnov, A., Holben, B. N., King, M. D., Kaufman, Y. J., Eck, T. F., and Slutsker, I.: Accuracy assessment of aerosol optical properties retrieval from AERONET sun and sky radiance measurements, J. Geophys. Res., 105, 9791–9806, https://doi.org/10.1029/2000JD900040, 2000.

Forrister, H., Liu, J., Scheuer, E., Dibb, J., Ziemba, L., Thornhill, K. L., Anderson, B., Diskin, G., Perring, A. E., Schwarz, J. P., Campuzano-Jost, P., Day, D. A., Palm, B. B., Jimenez, J. L., Nenes, A., and Weber, R. J.: Evolution of brown carbon in wildfire plumes. Geophys. Res. Lett., 42, 4623–4630. https://doi.org/10.1002/2015GL063897, 2015.

Froyd, K. D., Murphy, D. M., Brock, C. A., Campuzano-Jost, P., Dibb, J. E., Jimenez, J.-L., Kupc, A., Middlebrook, A. M., Schill, G. P., Thornhill, K. L., Williamson, C. J., Wilson, J. C., and Ziemba, L. D.: A new method to quantify mineral dust and other aerosol species from aircraft platforms using single-particle mass spectrometry, Atmos. Meas. Tech., 12, 6209–6239, https://doi.org/10.5194/amt-12-6209-2019, 2019.

Gao, R., Schwarz, J., Kelly, K., Fahey, D., Watts, L, Thompson, T., Spackman, R., Slowik, J. G., Cross, E. S., Han, J.-H., Davidovits, P., Onasch, T. B., and Worsnop, D.: A novel method for estimating light-scattering properties of soot aerosols using a modified single-particle soot photometer, Aerosol Sci. Tech., 41, 125-135, doi:10.1080/02786820601118398, 2007.

Guo, H., Campuzano-Jost, P., Nault, B. A., Day, D. A., Schroder, J. C., Dibb, J. E., Dollner, M., Weinzierl, B., and Jimenez, J. L.: The importance of size ranges in aerosol instrument intercomparisons: A case study for the ATom Mission, Atmos. Meas. Tech. Discuss., https://doi.org/10.5194/amt-2020-224, in review, 2020.

Haywood, J. M., Ramaswamy, V., and Soden, B. J.: Tropospheric aerosol climate forcing in clear-sky satellite observations over the oceans, Science, 283, 1299-1303, https://doi.org/10.1126/science.283.5406.1299, 1999.

Hess, M., Koepke, P., and Schult, I.: Optical properties of aerosols and clouds: The software package OPAC. Bull. Amer. Meteor. Soc., 79, 831–844, https://doi.org/10.1175/1520-0477(1998)079<0831:OPOAAC>2.0.CO;2, 1998.

Hodzic, A., Campuzano-Jost, P., Bian, H., Chin, M., Colarco, P. R., Day, D. A., Froyd, K. D., Heinold, B., Jo, D. S., Katich, J. M., Kodros, J. K., Nault, B. A., Pierce, J. R., Ray, E., Schacht, J., Schill, G. P., Schroder, J. C., Schwarz, J. P., Sueper, D. T., Tegen, I., Tilmes, S., Tsigaridis, K., Yu, P., and Jimenez, J. L.: Characterization of organic aerosol across the global remote troposphere: a comparison of ATom measurements and global chemistry models, Atmos. Chem. Phys., 20, 4607–4635, https://doi.org/10.5194/acp-20-4607-2020, 2020.

Holben B. N., Eck, T. F., Slutsker, I., Tanre, D., Buis, J. P., Setzer, A., Vermote, E., Reagan, J. A., Kaufman, Y., Nakajima, T., Lavenu, F., Jankowiak, I. and Smirnov, A.: AERONET - A federated instrument network and data archive for aerosol characterization, Remote Sens. Environ., 66, 1-16, https://doi.org/10.1016/S0034-4257(98)00031-5, 1998.

Holben, B. N., Eck, T. F., Slutsker, I., Smirnov, A., Sinyuk, A., Schafer, J., Giles, D., and Dubovik O.: AERONET's Version 2.0 quality assurance criteria, http://aeronet.gsfc.nasa.gov/new_web/Documents/ AERONETcriteria_final1.pdf (last access: 6 October 2020), 2006.

Hudson, P. K., Murphy, D. M., Cziczo, D. J., Thomson, D. S., de Gouw, J. A., Warneke, C., Holloway, J., Jost, H.

1040   J., and Hübler, G.: Biomass-burning particle measurements: Characteristics composition and chemical processing, J.

Geophys. Res.-Atmos., 109, D23S27, https://doi.org/10.1029/2003JD004398, 2004.

IPCC, Climate Change 2013: The Physical Science Basis. Contribution of Working Group I to the Fifth Assessment

Report of the Intergovernmental Panel on Climate Change, Stocker, T.F., Qin, D., Plattner, G.-K., Tignor, M., Allen, S. K.,

Boschung, J., Nauels, A., Xia, Y., Bex, V., and Midgley, P. M. (eds.), Cambridge University Press, Cambridge, United

1045   Kingdom and New York, NY, USA, 1535 pp., 2013.

Jimenez, J. L., Campuzano-Jost, P., Day, D. A., Nault, B. A., Guo, H., Schroder, J. C., and Cubison, M. J.:

Frequently AMS Questions for AMS Data Users, http://cires1.colorado.edu/jimenez-

group/wiki/index.php/FAQ_for_AMS_Data_Users, accessed 20 Jan. 2021.

Kahn, R. A., Berkoff, T. A., Brock, C., Chen, G., Ferrare, R. A., Ghan, S., Hanisco, T. F, Hegg, D. A., Martins, J.

1050   V., McNaughton, C. S., Murphy, D. M., Ogren, J. A., Penner, J. E., Pilewskie, P., Seinfeld, J. H., and Worsnop, D. R.: SAM-

CAAM: A concept for acquiring systematic aircraft measurements to characterize aerosol air masses, Bull. Am. Meteor.

Soc., 98, 2215-2228, https://doi.org/10.1175/BAMS-D-16-0003.1, 2017.

Katich, J. M., Samset, B. H., Bui, T. P., Dollner, M., Froyd, K., Campuzano-Jost, P., Nault, B., Schroder, J.,

Weinzierl, B., and Schwarz, J. P.: Strong contrast in remote black carbon aerosol loadings between the Atlantic and Pacific

1055   basins, J. Geophys. Res., 123, 13386-13395,doi:10.1029/2018JD029206, 2018.

Koepke, P., Gasteiger, J., and Hess, M.: Technical Note: Optical properties of desert aerosol with non-spherical

mineral particles: data incorporated to OPAC, Atmos. Chem. Phys., 15, 5947–5956, https://doi.org/10.5194/acp-15-5947-

2015, 2015.

Kuang, Y., Zhao, C., Tao, J., Bian, Y., Ma, N., and Zhao, G.: A novel method for deriving the aerosol

1060   hygroscopicity parameter based only on measurements from a humidified nephelometer system, Atmos. Chem. Phys., 17,

6651–6662, https://doi.org/10.5194/acp-17-6651-2017, 2017.

Kupc, A., Williamson, C., Wagner, N. L., Richardson, M., and Brock, C. A.: Modification, calibration, and performance of the Ultra-High Sensitivity Aerosol Spectrometer for particle size distribution and volatility measurements during the Atmospheric Tomography Mission (ATom) airborne campaign, Atmos. Meas. Tech., 11, 369–383,
1065   https://doi.org/10.5194/amt-11-369-2018, 2018.

Lack, D. A., Cappa, C. D., Langridge, J., Richardson, M., Law, D., McLaughlin, R. and Murphy, D. M.: Aircraft instrument for comprehensive characterisation of aerosol optical properties, Part 2: Black and brown carbon absorption and absorption enhancement measured with photo acoustic spectroscopy, Aerosol Sci. Technol. 45, 555-568, https://doi.org/10.1080/02786826.2011.645955, 2012.

1070   Langridge, J., Richardson, M., Lack, D. A., Law, D. and Murphy, D. M. : Aircraft instrument for comprehensive characterisation of aerosol optical properties, Part I: Wavelength dependent optical extinction and its relative humidity dependence measured using cavity ringdown spectroscopy, Aerosol Sci. Technol. 45, 1305-1318, https://doi.org/10.1080/02786826.2011.592745, 2011

Liu, D., He, C., Schwarz, J. P. and Wang, X.: Lifecycle of light-absorbing carbonaceous aerosols in the atmosphere,
1075   npj Clim. Atmos. Sci. 3, 40, https://doi.org/10.1038/s41612-020-00145-8, 2020.

Liu, X., Easter, R. C., Ghan, S. J., Zaveri, R., Rasch, P., Shi, X., Lamarque, J.-F., Gettelman, A., Morrison, H., Vitt, F., Conley, A., Park, S., Neale, R., Hannay, C., Ekman, A. M. L., Hess, P., Mahowald, N., Collins, W., Iacono, M. J., Bretherton, C. S., Flanner, M. G., and Mitchell, D.: Toward a minimal representation of aerosols in climate models: description and evaluation in the Community Atmosphere Model CAM5, Geosci. Model Dev., 5, 709–739,
1080   https://doi.org/10.5194/gmd-5-709-2012, 2012.

Liu, X., Ma, P.-L., Wang, H., Tilmes, S., Singh, B., Easter, R. C., Ghan, S. J., and Rasch, P. J.: Description and evaluation of a new four-mode version of the Modal Aerosol Module (MAM4) within version 5.3 of the Community Atmosphere Model, Geosci. Model Dev., 9, 505–522, https://doi.org/10.5194/gmd-9-505-2016, 2016.

Mann, G. W., Carslaw, K. S., Spracklen, D. V., Ridley, D. A., Manktelow, P. T., Chipperfield, M. P., Pickering, S.

1085   J., and Johnson, C. E.: Description and evaluation of GLOMAP-mode: a modal global aerosol microphysics model for the

UKCA composition-climate model, Geosci. Model Dev., 3, 519–551, https://doi.org/10.5194/gmd-3-519-2010, 2010.

McComiskey, A., Schwartz, S. E., Schmid, B., Guan, H., Lewis, E. R., Ricchiazzi, P. and Ogren, J. A.: Direct

aerosol forcing: Calculation from observables and sensitivities to inputs, J. Geophys. Res, 113,

D09202,https://doi.org/doi:10.1029/2007JD009170, 2008.

1090   McManus, J. B., Nelson, D. D., Shorter, J. H., Jimenez, R., Herndon, S., Saleska, S. R., and Zahniser, M. S.: A high

precision pulsed quantum cascade laser spectrometer for measurements of stable isotopes of carbon dioxide, J. Mod. Optic.,

52, 2309-2321, 2005.

McMurry, P. H and Wilson, J. C.: Growth laws for the formation of secondary ambient aerosols: Implications for

chemical conversion mechanisms, Atmos. Environ., 16, 121-134, https://doi.org/10.1016/0004-6981(82)90319-5, 1982.

1095   McNaughton, C. S., Clarke, A. D., Howell, S. G., Pinkerton, M., Anderson, B., Thornhill, L., Hudgins, C.,

Winstead, E., Dibb, J. E., Scheuer, E., and Maring, H.: Results from the DC-8 Inlet Characterization Experiment (DICE):

Airborne versus surface sampling of mineral dust and sea salt aerosols, Aerosol Sci. Technol., 41, 136–159,

https://doi.org/10.1080/02786820601118406, 2007.

Moteki, N., Kondo, Y. and Nakamura, S.: Method to measure refractive indices of small nonspherical particles:

1100   Application to black carbon particles, J. Aerosol Sci., 41, 513–521, doi:10.1016/j.jaerosci.2010.02.013, 2010.

Murphy, D. M., Cziczo, D. J., Hudson, P. K., Thomson, D. S., Wilson, J. C., Kojima, T., and Buseck, P. R.: Particle

generation and resuspension in aircraft inlets when flying in clouds, Aerosol Sci. Tech., 38, 401–409,

https://doi.org/10.1080/02786820490443094, 2004.

Murphy, D. M., Cziczo, D. J., Froyd, K. D., Hudson, P. K., Matthew, B. M., Middlebrook, A. M., Peltier, R. E.,

1105   Sullivan, A., Thomson, D. S., and Weber, R. J.: Single-particle mass spectrometry of tropospheric aerosol particles, J.

Geophys. Res., 111, D23S32, doi:10.1029/2006JD007340, 2006.

Murphy, D. M., Froyd, K. D., Apel, E., Blake, D., Blake, N., Evangeliou, N., Hornbrook, S., Peischl, J., Ray, E., Ryerson, T. B., Thompson, C., and Stohl, A.: An aerosol particle containing enriched uranium encountered in the remote upper troposphere, J. Environ. Radioactivity, 184-185, 95-100, doi:10.1016/j.jenvrad.2018.01.006, 2018.

1110   Murphy, D. M., Froyd, K. D., Bourgeois, I., Brock, C. A., Kupc, A., Peischl, J., Schill, G. P., Thompson, C. R., Williamson, C. J., and Yu, P.: Radiative and chemical implications of the size and composition of aerosol particles in the existing or modified global stratosphere, Atmos. Chem. Phys. Discuss., https://doi.org/10.5194/acp-2020-909, in review, 2020.

Nakao, S.: Why would apparent κ linearly change with O/C? Assessing the role of volatility, solubility, and surface 1115   activity of organic aerosols, Aerosol Sci. Technol., 51, 1377-1388,https://doi.org/10.1080/02786826.2017.1352082, 2017.

NASA: NASA Armstrong Fact Sheet: DC-8 Airborne Science Laboratory, https://www.nasa.gov/centers/armstrong /news/FactSheets/FS-050-DFRC.html, (last access: 6 October 2020), 2015.

Nault, B. A., Campuzano-Jost, P., Day, D. A., Jo, D. S., Schroder, J. C., Allen, H. M., Bahreini, R., Bian, H., Blake, D. R., Chin, M., Clegg, S. L., Colarco, P. R., Crounse, J. D., Cubison, M. J., DeCarlo, P. F., Dibb, J. E., Diskin, G. S., 1120   Hodzic, A., Hu, W., Katich, J. M., Kim, M. J., Kodros, J. K., Kupc, A., Lopez-Hilfiker, F. D., Marais, E. A., Middlebrook, A. M., Neuman, J. A., Nowak, J. B., Palm, B. B., Paulot, F., Pierce, J. R., Schill, G. P., Scheuer, E., Thornton, J. A., Tsigaridis, K., Wennberg, P. O., Williamson, C. J., and Jimenez, J. L.: Models underestimate the increase of acidity with remoteness biasing radiative impact calculations, Commun. Earth Environ., Submitted, Sep. 2020.

Park, K., D. B. Kittelson, M. R. Zachariah, and P. H. McMurry, Measurement of inherent material density of 1125   nanoparticle agglomerates, J. Nanopart. Res., 6, 267-272, 2004.

Petters, M. D. and Kreidenweis, S. M.: A single parameter representation of hygroscopic growth and cloud condensation nucleus activity, Atmos. Chem. Phys., 7, 1961–1971, doi:10.5194/acp-7-1961-2007, 2007.

Podolske, J. R., Sachse, G. W., and Diskin, G. S.: Calibration and data retrieval algorithms for the NASA Langley/Ames diode laser hygrometer for the NASA Transport and Chemical Evolution Over the Pacific (TRACE-P) 1130   mission, J. Geophys. Res., 108.8792, https://doi.org/10.1029/2002JD003156, 2003.

Quinn, P. K., Coffman, D. J., Johnson, J. E., Upchurch, L. M., and Bates, T. S.: Small fraction of marine cloud condensation nuclei made up of sea spray aerosol, Nature Geosci. 10, 674–679, https://doi.org/10.1038/ngeo3003, 2017.

Radke, L. F., Stith, J. L, Hegg, D. A., and Hobbs, P. V., Airborne studies of particles and gases from forest fires, J. Air Poll. Control Assoc., 28, 30-34, https://doi.org/10.1080/00022470.1978.10470566, 1977.

1135   Rickards, A. M. J., Miles, R. E. H., Davies, J. F., Marshall, F. H., and Reid, J. P.: Measurements of the sensitivity of aerosol hygroscopicity and the κ parameter to the O/C ratio, J. Phys. Chem. A, 117, 14120–14131, https://doi.org/10.1021/jp407991n, 2013.

Ryerson, T. B., Buhr, M. P., Frost, G. J., Goldan, P. D., Holloway, J. S., Hübler, G., Jobson, B. T., Kuster, W. C., McKeen, S. A., Parrish, D. D., Roberts, J. M., Sueper, D. T., Trainer, M., Williams, J., and Fehsenfeld, F. C.: Emissions

1140 lifetimes and ozone formation in power plant plumes, J. Geophys. Res., 103, 22569– 22583, doi:10.1029/98JD01620, 1998.

Schill, G. P., Froyd, K. D., Bian, H., Kupc, A., Williamson, C., Brock, C. A. Ray, E., Hornbrook, R. S., Hills, A. J., Apel, E. C., Chin, M., Colarco, P. R., and Murphy, D. M.: Widespread biomass burning smoke throughout the remote troposphere, Nat. Geosci. 13, 422–427, https://doi.org/10.1038/s41561-020-0586-1, 2020.

Schroder, J. C., Campuzano-Jost, P., Day, D. A., Shah, V., Larson, K., Sommers, J. M., Sullivan, A. P., Campos, T.,

1145 Reeves, J. M., Hills, A., Hornbrook, R. S., Blake, N. J., Scheuer, E., Guo, H., Fibiger, D. L., McDuffie, E. E., Hayes, P. L., Weber, R. J., Dibb, J. E., Apel, E. C., Jaeglé, L., Brown , S. S., Thornton, J. A., and Jimenez, J. L.: Sources and secondary production of organic aerosols in the northeastern United States during WINTER. J. Geophys. Res., Atmospheres, 123, 7771– 7796, https://doi.org/10.1029/2018JD028475, 2018.

Schwarz, J. P., Spackman, J. R., Gao, R. S., Perring, A. E., Cross, E., and Onasch, T. B., et al.: The detection

1150 efficiency of the single particle soot photometer, Aerosol Sci. Technol., 44, 612–628, https://doi.org/10.1080/02786826.2010.481298, 2010.

Scott, T., Bui, R. Chan, and Bowen, S. W.: The Meteorological Measurement System on the NASA ER-2 aircraft, J. Atmos. Oceanic Technol., 7, 525-540, https://doi.org/10.1175/1520-0426(1990)007<0525:TMMSOT>2.0.CO;2, 1990.

Shen, Y., Virkkula, A., Ding, A., Luoma, K., Keskinen, H., Aalto, P. P., Chi, X., Qi, X., Nie, W., Huang, X., Petäjä,

1155 T., Kulmala, M., and Kerminen, V.-M.: Estimating cloud condensation nuclei number concentrations using aerosol optical

properties: role of particle number size distribution and parameterization, Atmos. Chem. Phys., 19, 15483–15502,

https://doi.org/10.5194/acp-19-15483-2019, 2019.

Spanu, A., Dollner, M., Gasteiger, J., Bui, T. P., and Weinzierl, B.: Flow-induced errors in airborne in-situ

measurements of aerosols and clouds, Atmos. Meas. Tech., 13, 1963-1987, https://doi.org/10.5194/amt-13-1963-2020, 2020.

1160 Strode, S., Liu, J., Lait, L. R., Commane, R., Daube, B., Wofsy, S. C., Conaty, A., Newman, P., and Prather, M.:

Forecasting carbon monoxide on a global scale for the ATom-1 aircraft mission: insights from airborne and satellite

observations and modeling, Atmos. Chem. Phys., 18, 10955-10971, doi:10.5194/acp-18-10955-2018, 2018.

Thomson, D. S., Schein, M. E., and Murphy, D. M.: Particle analysis by laser mass spectrometry WB-57F

instrument overview, Aerosol Sci. Tech., 33, 153–169, https://doi.org/10.1080/027868200410903, 2000.

1165 Titos, G., Cazorla, A., Zieger, P., Andrews, E., Lyamani, H., Granados-Muñoz, M. J., Olmo, F. J., and Alados-

Arboledas, L.: Effect of hygroscopic growth on the aerosol light-scattering coefficient: A review of measurements,

techniques and error sources, Atmos. Environ., 141, 494-507, https://doi.org/10.1016/j.atmosenv.2016.07.021, 2016.

Walser, A., Sauer, D., Spanu, A., Gasteiger, J., and Weinzierl, B.: On the parametrization of optical particle counter

response including instrument-induced broadening of size spectra and a self-consistent evaluation of calibration

1170 measurements, Atmos. Meas. Tech., 10, 4341–4361, https://doi.org/10.5194/amt-10-4341-2017, 2017.

Washenfelder, R. A., Attwood, A. R., Brock, C. A., Guo, H., Xu, L., Weber, R. J., Ng, N. L., Allen, H. M., Ayres,

B. R., Baumann, K., Cohen, R. C., Draper, D. C., Duffey, K. C., Edgerton, E., Fry, J. L., Hu, W. W., Jimenez, J. L., Palm, B.

B., Romer, P., Stone, E. A., Wooldridge, P. J., and Brown, S. S.: Biomass burning dominates brown carbon absorption in the

rural southeastern United States, Geophys. Res. Lett., 42, 653–664, doi:10.1002/2014GL062444, 2015.

1175 Williamson, C., Kupc, A., Wilson, J., Gesler, D. W., Reeves, J. M., Erdesz, F., McLaughlin, R., and Brock, C. A.:

Fast time response measurements of particle size distributions in the 3–60 nm size range with the nucleation mode aerosol

size spectrometer, Atmos. Meas. Tech., 11, 3491–3509, https://doi.org/10.5194/amt-11-3491-2018, 2018.

Williamson, C. J., Kupc, A., Axisa, A., Kelsey R., Bilsback, K. R, Bui, T. P., Campuzano-Jost, P., Dollner, M., Froyd, K. D., Hodshire, A. L., Jimenez, J. L., Kodros, J. K., Luo, G., Murphy, D. M., Nault, B. A., Ray, E. A., Weinzierl, B.,

1180   Wilson, J. C., Yu, F., Yu, P., Pierce, J. R., and Brock, C. A.: A large source of cloud condensation nuclei from new particle formation in the tropics, Nature 574, 399–403, https://doi.org/10.1038/s41586-019-1638-9, 2019.

Wofsy S. C.: HIAPER Pole-to-Pole Observations (HIPPO): Fine-grained, global-scale measurements of climatically important atmospheric gases and aerosols, Phil. Trans. R. Soc. A., 369, 2073–2086, http://doi.org/10.1098/rsta.2010.0313, 2011.

1185   Wofsy, S. C., and 105 co-authors: ATom: Merged Atmospheric Chemistry, Trace Gases, and Aerosols [dataset]. ORNL DAAC, Oak Ridge, Tennessee, USA. https://doi.org/10.3334/ORNLDAAC/158, 2018.

Zaveri, R. A.: A new method for multicomponent activity coefficients of electrolytes in aqueous atmospheric aerosols, J. Geophys. Res., 110, D02201, doi:10.1029/2004JD004681, 2005.

Zeng, L., Zhang, A., Wang, Y., Wagner, N. L., Katich, J. M., Schwarz, J. P., Schill, G. P., Brock, C., Froyd, K. D.,

1190   Murphy, D. J., Williamson, C. J., Kupc, A., Scheuer, E., Dibb, J. and Weber, R. J.: Global measurements of brown carbon and estimated direct radiative effects, Geophys. Res. Lett., 47, e2020GL088747, https://doi.org/10.1029/2020GL088747, 2020.